atmosphere

MDPI

Article

Estimating the Effects of Climate Fluctuations on Precipitation and Temperature in East Africa

Edovia Dufatanye Umwali [1,2,3,4,5], Xi Chen [1,2,3,5,6,*], Brian Odhiambo Ayugi [7], Richard Mumo [8], Hassen Babaousmail [9], Dickson Mbigi [3,10] and David Izere [1,3,4,5]

1 Xinjiang Institute of Ecology and Geography, Chinese Academy of Sciences, 818 South Beijing Road, Urumqi 830011, China; umwariedovia@mails.ucas.ac.cn (E.D.U.); izerarmand@gmail.com (D.I.)
2 Xinjiang Key Laboratory of RS & GIS Application, Urumqi 830011, China
3 University of Chinese Academy of Sciences, Beijing 100039, China; dickson.mbigi@gmail.com
4 Faculty of Environmental Sciences, University of Lay Adventists of Kigali (UNILAK), Kigali P.O Box 6392, Rwanda
5 Joint Research Center for Natural Resources and Environment in East Africa, Kigali P.O. Box 6392, Rwanda
6 Zhejiang University of Technology, No.18, Chaowang Road, Hangzhou 310023, China
7 East Africa Hub, Wyss Academy for Nature at the University of Bern, Nanyuki P.O. Box 11866-00400, Kenya; bayugi@seoultech.ac.kr
8 Department of Mathematics and Statistical Sciences, Botswana International University of Science and Technology, Private Bag 16, Palapye Plot 10071, Botswana; kitatimumo@gmail.com
9 School of Atmospheric Science and Remote Sensing, Wuxi University, Wuxi 214105, China; baw.hassan47@gmail.com
10 Department of Physics, University of Dar es Salaam, Dar es Salaam P.O. Box 35063, Tanzania
* Correspondence: chenxi@ms.xjb.ac.cn

Abstract: This study evaluated the effectiveness of the NASA Earth Exchange Global Daily Downscaled models from CMIP6 experiments (hereafter; NEX-GDDP-CMIP6) in reproducing observed precipitation and temperature across East Africa (EA) from 1981 to 2014. Additionally, climate changes were estimated under various emission scenarios, namely low (SSP1-2.6), medium (SSP2-4.5), and high (SSP5-8.5) scenarios. Multiple robust statistics metrics, the Taylor diagram, and interannual variability skill (IVS) were employed to identify the best-performing models. Significant trends in future precipitation and temperature are evaluated using the Mann-Kendall and Sen's slope estimator tests. The results highlighted IPSL-CM6A-LR, EC-Earth3, CanESM5, and INM-CM4-8 as the best-performing models for annual and March to May (MAM) precipitation and temperature respectively. By the end of this century, MAM precipitation and temperature are projected to increase by 40% and 4.5 °C, respectively, under SSP5-8.5. Conversely, a decrease in MAM precipitation and temperature of 5% and 0.8 °C was projected under SSP2-4.5 and SSP1-2.6, respectively. Long-term mean precipitation increased in all climate scenarios (SSP1-2.6, SSP2-4.5, and SSP5-8.5), with near-term MAM precipitation showing a 5% decrease in Rwanda, Burundi, Uganda, and some parts of Tanzania. Under the SSP5-8.5 scenario, temperature rise exceeded 2–6 °C in most regions across the area, with the fastest warming trend of over 6 °C observed in diverse areas. Thus, high greenhouse gas (GHG) emission scenarios can be very harmful to EA and further GHG control is needed.

Keywords: East Africa; MME; NEX-GDDP-CMIP6; precipitation; temperature

Citation: Dufatanye Umwali, E.; Chen, X.; Odhiambo Ayugi, B.; Mumo, R.; Babaousmail, H.; Mbigi, D.; Izere, D. Estimating the Effects of Climate Fluctuations on Precipitation and Temperature in East Africa. *Atmosphere* **2024**, *15*, 1455. https://doi.org/10.3390/atmos15121455

Academic Editor: Andreas Matzarakis

Received: 22 October 2024
Revised: 3 December 2024
Accepted: 3 December 2024
Published: 5 December 2024

1. Introduction

Climate change has become a great concern among climate researchers in recent years [1,2]. The IPCC Fifth Assessment Report (AR5) [3,4] noted that a 0.85 ± 0.21 °C increase in global surface warming occurred from 1880 to 2012, with the past three decades showing the largest increase. This has resulted in frequent occurrences of extreme climate events like droughts and floods, among others [5]. The associated influences of increased extreme climate actions include changes in the hydrological cycle, agriculture production,

ecosystem services, and the socioeconomic system [6]. The future prospect indicates more frequent extreme climate events with vigorous intensity, severity, and longer periods under various emission scenarios [7]. Different places are affected by climate change differently, although countries that are developing are those who suffer the most.

The African continent is notably one of the regions utmost susceptible to the effects of climate change owing to its elevated exposure and limited adaptation ability [8]. These adverse effects are perceived through the casualties emanating from the increased frequency and intensity of climate extremes across the continent. Over East Africa (EA), drylands in arid and semiarid regions are highly susceptible to experiencing severe climatic events [9] owing to the limited resources, rainfed agriculture, and significant water scarcity levels [10–12]. The incidences of extreme events in the region have shown devastating effects on the population and societal infrastructure [13,14]. Particularly, there has been a notable increase in the loss of lives, disturbance to livelihoods, damage to property, and societal unrest in the area [15]. It is predicted that future extremes will generate new threats that may have never been experienced in the recent past [16] and likewise will play a big role in the future loss of lives [17]. Hence, it is crucial to consider the model's performance as well as the past and future projections of precipitation and temperature, particularly focusing on the EA region.

Global Climate Models (GCMs) have been identified as the foremost numerical coupled models and reliable tools [18] for examining the climate change effects [19,20] on global as well as regional scales [21] and providing future climate predictions [22]. These models delivered from the Coupled Model Intercomparison Project (CMIP) overseen by the World Climate Research Program (WCRP) are aimed at analyzing and forecasting alterations in earth systems. Additionally, featured in the recently released CMIP6 [23], they have been broadly applied in previous research to forthcoming climate changes [24–26]. Besides, certain studies have indicated that CMIP6 models reveal a notable enhancement in simulating and predicting precipitation and temperature at large more reliably and accurately than CMIP5 and CMIP3 [27,28].

In the study area, several modeling studies have been conducted. Using CMIP5 models, refs. [29,30] examined the effectiveness of models in predicting variations in mean temperature and rainfall. This is the study that reported an augmentation in temperature and an increase in rainfall, which is projected to the end of this century. With the advent of CMIP6 models, numerous studies have been conducted over the EA region with a focus on simulating and projecting changes in extreme temperature and rainfall [31–33]. Their findings showed a rise in the number of continuous dry periods and a decline in the consecutive wet periods by the close of this century. The projections similarly indicated significant increasing tendencies in temperature, with larger warming in the latest CMIP6 models compared to their predecessors. Overall, the studies based on CMIP5/6 showed persistent biases in their performance and uncertainties in projecting future outcomes [34]. These uncertainties make a crucial challenge for accurately simulating climate in the EA region using GCMs. For instance, previous studies based on CMIP5 models reported a contrasting pattern of observed and projected changes in the March-April-May (MAM) season under future climate conditions [35–37]. This contrasting projection and observed changes in MAM rainfall, a term commonly known as the "EAn Climate Paradox" has continued to manifest in recently released CMIP6 models [31].

To enhance the investigation of the influence of climate change at regional levels, NASA undertook a project to improve the quality of the CMIP6. This involved downscaling the models through the daily application of the monthly bias correction/spatial disaggregation (BCSD) as well as refining their horizontal grid resolution to $0.25^\circ \times 0.25^\circ$ [38]. Presently, the NEX-GDDP-CMIP6 models have 8 variables from 5 CMIP6 experiments (historical, SSP1-2.6, SSP2-4.5, SSP3-7.0, and SSP5-8.5) and are accessible from 35 GCMs. Consequently, numerous studies have been implemented to affirm the robustness of the NEX-GDDP-CMIP6 models' performances over different regions [39–41]. To the best of our knowledge, no relevant evaluation studies have assessed the robustness of NEX-GDDP-CMIP6 models

and explored possible future climate changes over the EA region. An extensive estimation of NEX-GDDP-CMIP6's performance in assessing past and future precipitation and temperature is essential to strengthen confidence in future climate projections.

Hence, this study aims to estimate the model effectiveness and the ability of the updated GCM outputs from CMIP6 to simulate annual and MAM precipitation and temperature changes. This assessment was conducted under various SSP scenarios including SSP1-2.6, SSP2-4.5, and SSP5-8.5. Specifically, the focus is on evaluating the capability of a multi-model ensemble of NEX-GDDP-CMIP6 in simulating annual and MAM climatology. Subsequently, to examine the projected changes in precipitation and temperature under various SSP scenarios. Advancing our understanding regarding simulated and projected precipitation and temperature conditions would have great significance for society and policy planning.

2. Materials and Methods

2.1. Study Area Description

The East Africa (EA) region comprises 5 countries, namely, Kenya, Uganda, Tanzania, Burundi, and Rwanda (Figure 1). It is enclosed within a geographical longitude of 28°00′00″ to 42°00′00″ E and latitude of 12°00′00″ S to 5°00′00″ N [42]. This region is distinguished by notable physiographic features, including Lake Victoria, which is shared among Kenya (6%), Uganda (45%), and Tanzania (49%). As the largest Lake in Africa, Lake Victoria, along with other sizable inland water bodies, plays a role in regulating moisture distribution in the region [43] and serves as a vital livelihood for the population of the region [44]. Additionally, this region boasts prominent geographical landmarks such as the Rif Valley and Africa's highest elevations, including Mt. Kilimanjaro (>5885 m), Mt. Kenya (>5199 m), and Mt. Ruwenzori (>5109 m) [31]. These characteristics significantly impact the regional weather and climate [45].

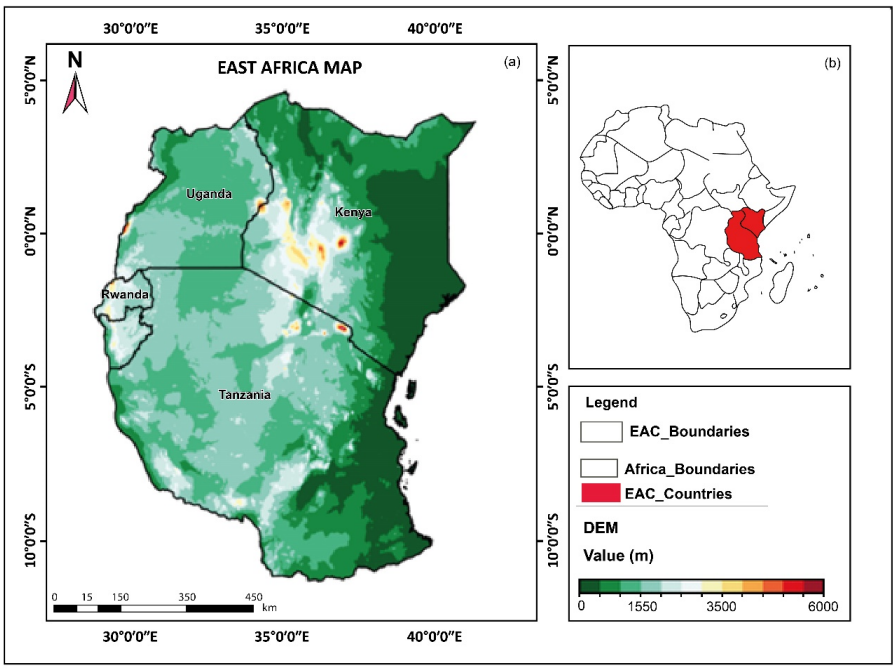

Figure 1. (**a**) Location of EA within longitude 28°00′00″ to 42°00′00″ E and latitude 12°00′00″ S to 5°00′00″ N with topographical distribution. (**b**) The relative location of EA over Africa is depicted on the top right insert of the African map with red color. The bottom right insert depicts the legend and color bar for the EA map (left column).

The study area has two main rainy seasons: the long rainy season occurs during MAM, whereas the short rainy season occurs during October-November-December (OND) [45].

Therefore, the study focused on the MAM season due to its high contribution to the annual total rains, an important agriculture season in most areas, and the EA climate paradox which is experienced in this season. The region mainly relies on an agro-based economy, where 80% of the population depends on rainfed agriculture for survival [46]. The emergence of extreme events like droughts and floods exacerbates the vulnerability of a population already grappling with abject poverty due to prevalent economic turmoil [47]. The mean annual precipitation varies from 800 to 1200 mm, displaying a considerable spatiotemporal distribution [48]. The region generally experiences warm temperatures year-round, with a range between 19 and 30 °C [49]. It is characterized by a climate typical of tropical savanna [50].

2.2. Observation and Model Datasets

The 21 historical models were used over EA (Table S1). The precipitation and temperature datasets were downloaded from the latest NEX-GDDP-CMIP6 dataset and took into consideration the first ensemble member 'r1i1p1f1' [23,38] across all the time frames. The dataset provides a finer spatial resolution of 0.25° × 0.25°, enhancing its ability to accurately depict climate change. This resolution has been approved through many studies [51–53]. Initially, the models underwent standardization for unit and calendar date formats at each timescale. The gridded precipitation and temperature dataset from the Climatic Research Unit (CRU version TS4.05) [54] was used owing to its quality and long time series. Additionally, various studies [55,56] have highlighted the low quality and limited duration of in situ weather records in EA. Despite these limitations, such as data have been widely utilized in climate change and ecological environment research [57]. Moreover, all the data were standard converted to a consistent grid using the bilinear interpolation method. The annual and MAM multi-model ensemble (MME) was used for all the models.

Firstly, the historical timeline (1981–2014) was used to evaluate the simulated spatiotemporal mean annual, MAM precipitation, temperature, MME, and CRU datasets. Moreover, for spatial comparison between observed and simulated data, the Taylor diagram was performed to depict the standard deviation (SD), correlation coefficient (CC), and root mean square difference (RMSD) [32,58–60]. The mathematical equations are expressed in Equations (1) and (2):

$$RMSD = \sqrt{\frac{1}{n}\sum_{i=1}^{n}(GCM_i - CRU_i)^2} \tag{1}$$

$$CC = \frac{\sum_{i=1}^{n}\left(CRU_i - \overline{O_i}\right)\left(GCM_i - \overline{GCM_i}\right)}{\sqrt{\sum_{i=1}^{n}\left(CRU_i - \overline{CRU_i}\right)^2\sum_{i=1}^{n}\left(GCM_i - \overline{GCM_i}\right)^2}} \tag{2}$$

where CRU represents observed values, GCMs refer to the model simulation, n denotes the number of pairs for the given period then i stands for observed and simulated pairs.

In addition, we used a Taylor diagram for the models ranking according to their performance. This diagram displays a comprehensive statistical summary illustrating the degree of similarity between a simulated pattern and an observed pattern. It effectively presents the RMSD, SD, and CC variations in the same diagram [61]. The formula for Taylor can be summarized in Equation (3):

$$X'^2 = \sigma_e^2 + \sigma_r^2 - 2\sigma e^{\sigma} r^{CC} \tag{3}$$

where the geometric relationship between the CC, the centered pattern RMS error X, and the standard deviations σ_e and σ_r of the test and reference fields, respectively. This method is widely utilized in many studies to evaluate the similarities between various data sets [62,63]. We employed this approach to estimate the effectiveness of CMIP6 models in assessing the spatial variations in precipitation and temperature across the study area.

On the other hand, the evaluation of the simulations' interannual variability in comparison to observations was conducted with the interannual variability skill score (IVS), which is calculated as Equation (4):

$$\text{IVS} = \left(\frac{STD_m}{STD_0} - \frac{STD_0}{STD_m}\right)^2 \quad (4)$$

where STD_m and STD_0 represent the standard deviations of the simulation and observation, respectively. The IVS statistic was employed to assess the similarity in interannual variation between simulations and observed. A more accurate interannual variability simulation is denoted by a lower IVS value. A value approaching zero signifies the improved performance of GCMs compared to the CRU data. To identify the significance of the trends, the modified Mann-Kendall (m-MK) test proposed by [64] was used. Despite this fact, using the Sen's Slope estimator the magnitude of trends in precipitation and temperature were estimated [65].

2.3. Projection Datasets

For this analysis, we opted for the five top-performing CMIP6 models within the shared socioeconomic pathways (SSP) scenarios, specifically SSP1-2.6, SSP2-4.5, and SSP5-8.5 (Table 1). The selected scenarios represent the low, medium, and high-emission scenarios, respectively. For projections, the first realization (r1i1p1f1) of models for both SSP scenarios was also selected. Hereafter, using the previously described methods, the models in every SSP scenario underwent standardization for unit scale and calendar date formats and were then adjusted to the uniform grid resolution. Referring to the historical period (1981–2014), we considered the near-term (2031–2065) and far-future (2066–2100) of the 21st century. Hence, for the analysis, the MME was developed for both near and far-term scenarios. Several studies stated that owing to the inherent uncertainties in individual GCMs, the use of MME yields more robust and reliable climate projections than the individual model [32,66,67]. For instance, refs. [59,68] used the MME approach with the best-performing models in their respective studies. Therefore, We applied the modified Mann-Kendall test (m-MK) [64] and Sen's Slope estimator [65] for trend detection analysis. Table 1 provides details about the chosen models for the analysis.

Table 1. List of the best models that are used to compute MME for future projections.

Precipitation		Temperature	
Annual	**MAM**	**Annual**	**MAM**
IPSL-CM6A-LR	CanESM3	EC-Earth3	INM-CM4-8
NESM3	BCC-CSM2-MR	NESM3	KIOST-ESM
MPI-ESM1-2-HR	IPSL-CM6A-LR	IPSL-CM6A-LR	CanESM5
CanESM5	NESM3	ACCESS-ESM1-5	NorESM2-MM
MIROC6	CMCC-ESM2	NorESM2-MM	INM-CM5-0

3. Results and Discussion

3.1. Climatology Spatiotemporal and Interannual Variability

Figure 2 illustrates the long-term mean precipitation and temperature from the chosen GCMs, MME, and reference (CRU) data for EA during the period 1981–2014. The CRU dataset registered an annual mean precipitation exceeding 80 mm and an annual mean temperature exceeding 23 °C over the area. Most models exhibit annual mean precipitation ranging from 70 and 85 mm and annual mean temperature between 24 and 27 °C. Among the selected models, MRI-ESM2-0 observed the highest values of annual mean precipitation, while the CMCC-CM2-SR5 observed the highest values of annual mean temperature. The NEX-GDDP-CMIP6 models from ACCESS-CM2, ACCESS-ESM1-5, BCC-CSM2-MR, CanESM5, CMCC-CM2-SR5, CMCC-ESM2, EC-Earth3-Veg-LR, INM-CM4-8, IPSL-CM6A-LR, KIOST-ESM, MIROC6, MPI-ESM1-2HR, MPI-ESM1-LR, MRI-ESM2-0, NorESM2-LM

and NorESM2-MM simulated annual mean precipitation at ≥80 mm. Conversely, models such as EC-Earth3, GDFL-ESM4, INM-CM5-0, KACE-1-0-G, and NESM3 models underestimated annual mean precipitation between 65 and 79 mm/month, respectively. For temperature analysis, all models simulate annual mean temperatures between 23 and 24 °C except CMCC-CM2-SR5, which produced 28 °C.

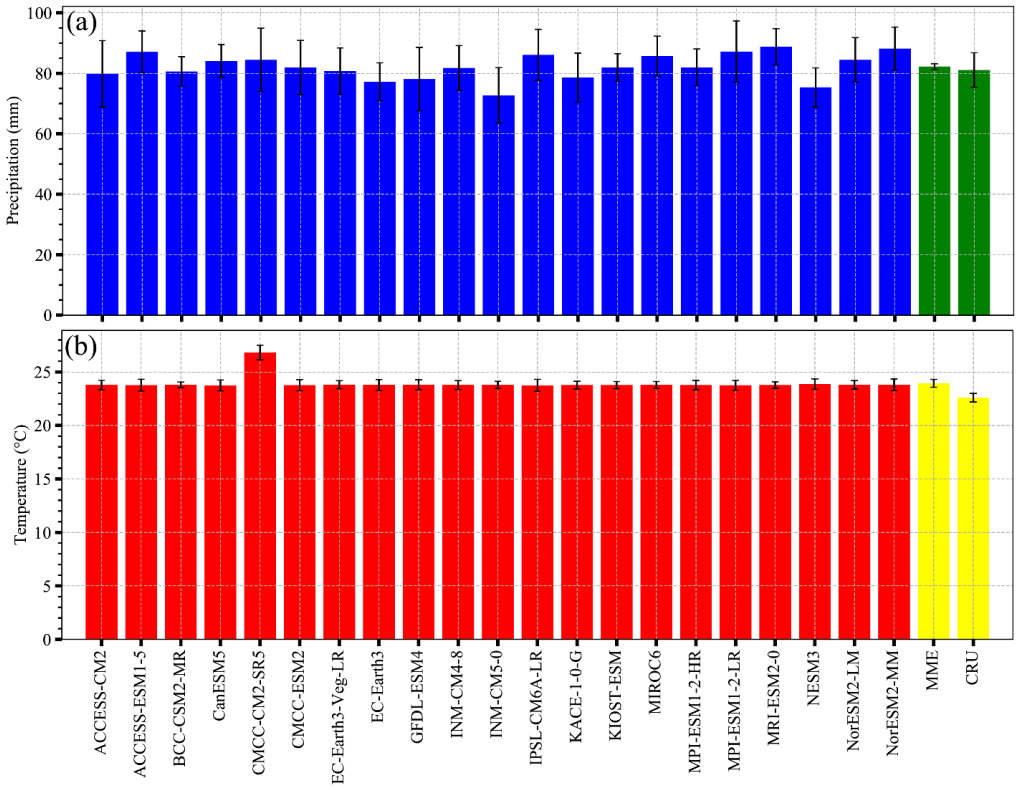

Figure 2. Long-term mean over EA during 1981–2014 (**a**) precipitation (units: mm) showing blue for CMIP6 models and green for MME and CRU observations and (**b**) temperature (units: °C) showing red for CMIP6 models and yellow for MME and CRU observations.

Past research has discovered that the performance of GCMs over the East A region has revealed a more prominent warming trend related to the observations [32,69]. This aligns with the findings of our study.

Figure 3a–f presented the spatial distributions of annual and MAM precipitation from observations, the MME, and simulation biases. For observations, results show a higher mean precipitation on the southern coast of Tanzania, encompassing the Lake Victoria region, covering most parts of Uganda, certain central areas of Kenya, and specific eastern regions of Tanzania during the MAM season (Figure 3b). In contrast, annual observation (Figure 3a) showed low mean precipitation in the central and northeast parts of Tanzania towards the southwest part of Kenya and a substantially low amount in the eastern and northern parts of this country. The small precipitation amounts in northern and eastern Kenya are mostly due to the spreading quasi-meridional low-level winds prevailing across the region [70,71]. Central Tanzania experiences dry precipitation due to the influence of topography and the absence of significant water bodies in the region [72]. This can lead to serious economic problems and ecological disasters with prolonged droughts in the region. Based on the models (Figure 3c,d), the MME mimics the observational results of the spatial precipitation distribution in most regions for both annual and MAM, indicating the great job done by the models to replicate precipitation patterns over EA. This is in parallel with the recent findings put forth by [73], although the authors use an ensemble of almost all CMIP6 models. Moreover, ref. [71] found the models failed to capture the

rainfall spatial distribution over the southeastern parts of the study region. This can be related to the fact that the authors used a few models to constitute the MME, and this implies the importance of considering large ensemble members to better simulate the spatial distribution of precipitation over EA. During the MAM (Figure 3f), the MME of the models overestimates the bias in the southeast part of the area, while during the annual (Figure 3e), the MME of the models tends to underestimate the bias over the region. The biases of the models are generally endorsed by their coarse resolution, preventing the accurate detection of the effects of topography and inadequate depiction of convective structures [68].

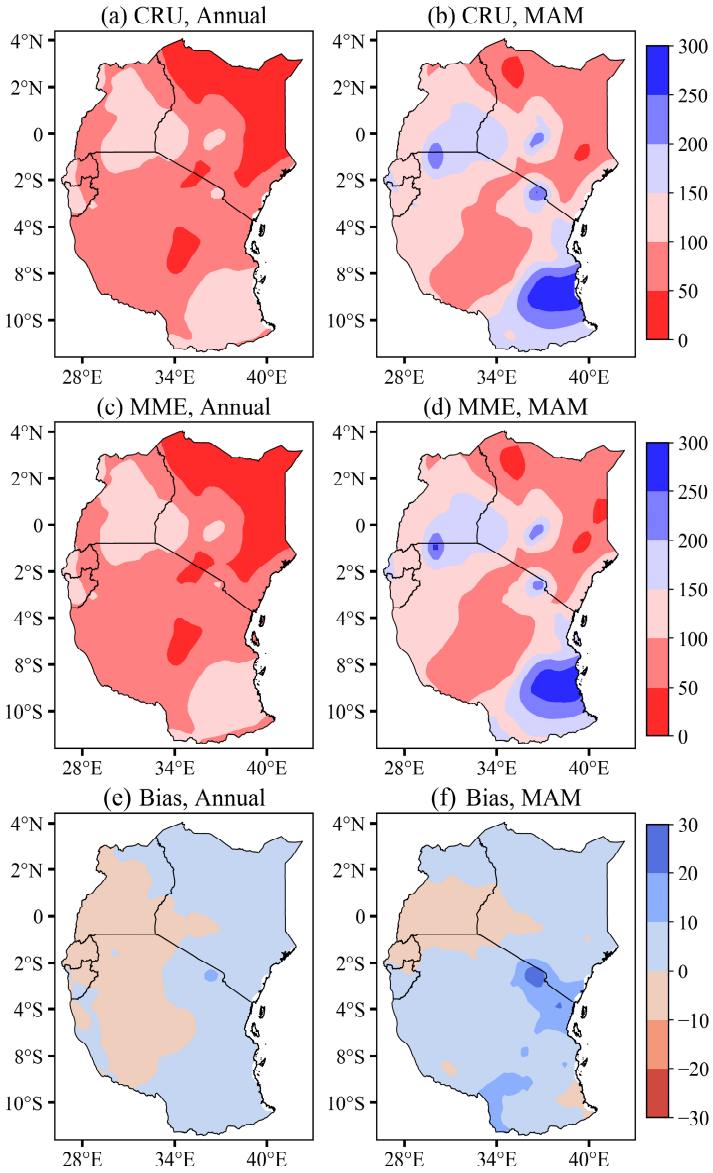

Figure 3. Spatial distributions of (**a**,**b**) observed precipitation (units: mm), (**c**,**d**) MME simulated precipitation (units: mm), and (**e**,**f**) biases in MME simulation compared to the observation (simulation minus observation, units: mm) for the period 1981–2014. The panels progress from the left to the right, representing annual and MAM, respectively. Note that the color bar scales vary across the panels.

The climatological spatial distributions of annual and MAM temperature from observations (CRU), the MME, and simulation biases in comparison to observation are presented in Figure 4a–f, respectively. For the observed MAM temperature (Figure 4b), the high-temperature patterns were found in the east part, especially the east-north and northwest

parts of Kenya. In contrast, the observed annual temperature (Figure 4a) showed low values around Lake Victoria. Notably, the area is climatologically dry, with a decrease in precipitation annually. In agreement with other studies, ref. [32] stated that at the end of 21st the century, regions of eastern Kenya anticipated a noticeable patch of warming of 0.8–1.4 °C. The MME overestimated the temperature in some parts of the area, especially in some eastern and northern parts of Kenya (Figure 4c,d). Consistent with the findings by [74], it was indicated that the eastern and northern parts experience the highest temperatures. These regions are categorized as low-lying regions, featuring arid and semi-arid climates along with scarce vegetation cover [75]. The bias generally falls below 0 °C in most areas but is underestimated in some parts of the area, such as the southern and eastern parts of Tanzania, the western part of Rwanda and Burundi, the eastern part of Uganda, and the eastern, northern, and middle parts of Kenya (Figure 4e,f). In contrast to the study by [32], which evaluated the historical mean surface temperature in the EA region using CMIP6 for the 21st century. Their findings revealed that the majority of models exhibited greater temperature variations over the western regions, including Uganda, Rwanda, Burundi, and parts of Tanzania. Ref. [76] state aerosol concentrations, surface-based feedback, an augmentation in the thermal radiation budget, escalating urbanization rates, and intensive changes in land use are explanatory factors that can explain the increase in temperature.

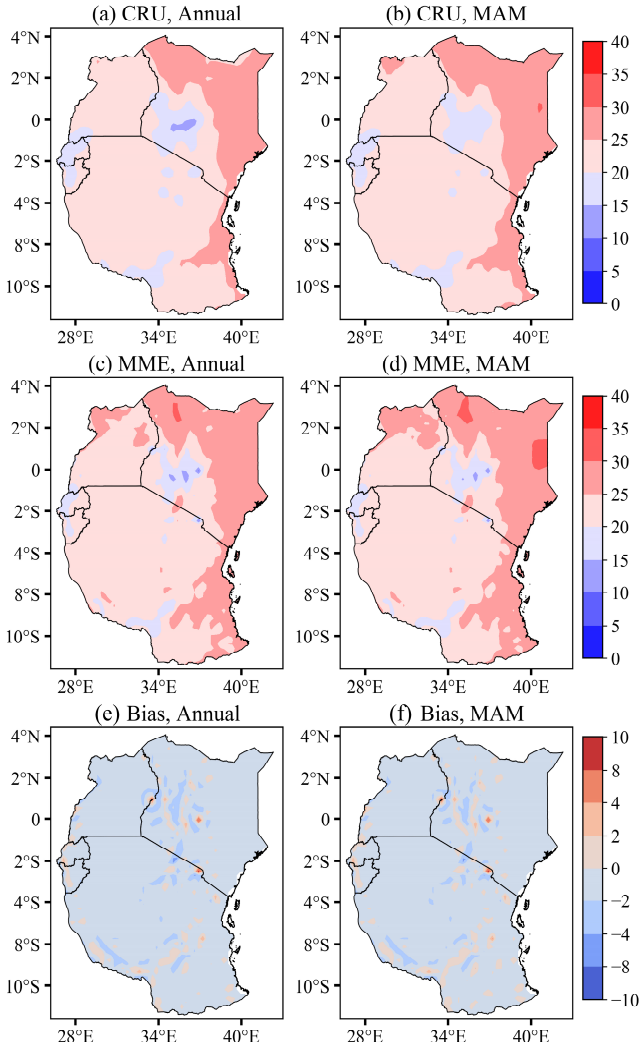

Figure 4. Spatial distributions of (**a**,**b**) observed temperature (units: °C), (**c**,**d**) MME simulated temperature (units: °C), and (**e**,**f**) biases in MME simulation compared to the observation (simulation minus observation, units: mm) for the period 1981–2014. The panels progress from the left to the right, representing annual and MAM, respectively. Note that the color bar scales vary across the panels.

3.2. Performance of Climate Models

The use of Taylor diagrams and a high spatial correlation coefficient has been proven to enhance the efficacy and precision of the selected climate models [77]. Figure 5 describes the Taylor diagrams representing annual and MAM precipitation and temperature over EA as replicated by 21 CMIP6 models and MME in comparison to observations from CRU. The correlation coefficients for annual and MAM precipitation vary from 0.7 to 0.95 and 0.2 to 0.7 (Figure 5a,c), respectively, while annual and MAM temperature vary from 0.6 to 0.95 and 0.5 to 0.8 (Figure 5b,d), respectively. This strong correlation demonstrates the models' aptitude to reliably depict the spatial and temporal distribution features of precipitation and temperature [77]. Nevertheless, the poorest availability of CRU data in Africa might be attributable to the low correlation coefficients [78,79]. Particularly, most of the models in MAM precipitation exhibited a low correlation coefficient ranging between 0.3 and 0.5 excluding INM-CM4-8 showed a weak correlation coefficient of 0.25. For instance, NESM3, MPI-ESM1-2-HR, GFDL-ESM4, IPSL-CM6A-LR, CMCC-CM2-SR5, ACCESS-CM2, NorESM2-LM, EC-Earth3-Veg-LR, ACCESS-ESM1-5, KACE-1-0-G and MPI-ESM1-2-LR. As for the RMSD of annual precipitation, most of the models fell within the range of 0.4 to 0.8 while for the MAM season, most of the models ranged from 1.0 to 1.5. Conversely, the RMSD for annual temperature across the utmost of the models varied between 0.5 to 0.7 while the MAM season ranged from 0.6 to 1.0. Generally, the MME for both precipitation and temperature exhibits better performance in the range between 0.7–0.95. Moreover, precipitation and temperature averaged annually performed better than that during MAM. Our findings agree with the previous study by [32] identified that the CMIP6 ensemble indicates vigorous simulations related to the individual with >0.90. Specifically, annual precipitation and temperature performed better than the MAM season. The majority of GCMs depict a larger SD in annual precipitation than observation, except BCC-CSM2-MR, CanESM5, GFDL-ESM4, NESM3, MPI-ESM1-2-HR, and IPSL-CM6A-LR, which reproduce a similar or smaller SD. While in MAM precipitation, BCC-CSM2-MR and CanESM5 only reproduce smaller SD. On the other hand, at annual temperature, NorESM2-LM and IPSL-CM6A-LR depict smaller SD while at the MAM temperature, CMCC-C2-SR5 showed the highest SD with 1.5. Particularly, most of the GCMs in MAM temperature depict smaller SD than observation, with only IPSL-CM6A-LR, NESM3, EC-Earth3, CMM-ESM2, EC-Earth3-Veg-LR, GFDL-ESM4, and ACCESS-CM2 reproducing similar or higher SD. In the MAM, the majority of precipitation models exhibit a larger bias, except for CanESM5, BCC-CSM2-MR, MRI-ESM2-0, and NorESM2-MM, whereas, in temperature, CMCC-CM2-SR5 shows a larger bias related to overestimations. In contrast to the annual precipitation and temperature, the findings indicate that during the study period, a majority of the models display a more robust correlation with observed data in MAM, demonstrating their virtuous performance and close agreement. In general, the MME shows robust simulations compared with individual models.

In general, some studies have shown that improved model resolution proved improved performance in replicating spatial patterns in observations across EA [23,32,80]. Compared to the previous studies globally in different domains, some indicate a slightly improved performance in CMIP6 in modeling climatic variables compared to CMIP5 [81–83]. Figure 6 illustrates the IVS values for the simulations of annual and MAM precipitation and temperature across the study area. The ideal model displays an IVS value that approaches zero. The outcomes indicated that the best models in annual precipitation were IPSL-CM6A-LR, NESM3 and CanESM5, BCC-CSM2-MR in MAM precipitation while for the temperatures, the best models were EC-Earth3 and INM-CM4-5, KIOST-ESM in annual and MAM temperature, respectively. Moreover, several models exhibited superior performance, attaining an IVS score below 0.3. Notable exceptions include NorESM2-LM, KIOST-ESM, MPI-ESM1-2-LR, EC-Earth3-Veg-LR, and KACE-1-0-G in MAM precipitation as well as CMCC-CM2-SR5 in MAM temperature. In contrast, the models demonstrate replicating the interannual variability of precipitation and temperature annually, outperforming their performance in MAM. Furthermore, it is noteworthy to highlight that a

considerable proportion of models show an IVS value within the acceptance range (≤1), signifying satisfactory performance concerning interannual variability [84]. Conclusively, all the models have better performance with IVS values below 0.9 for both precipitation and temperature and MME values less than 0.25. The MME simulates climate change more accurately than most individual models [85,86]. In the analysis, an MME was constructed to analyze future changes. Therefore, the best five models for annual and MAM precipitation and temperature have been selected to compute MME for projections of precipitation and temperature (Table 1).

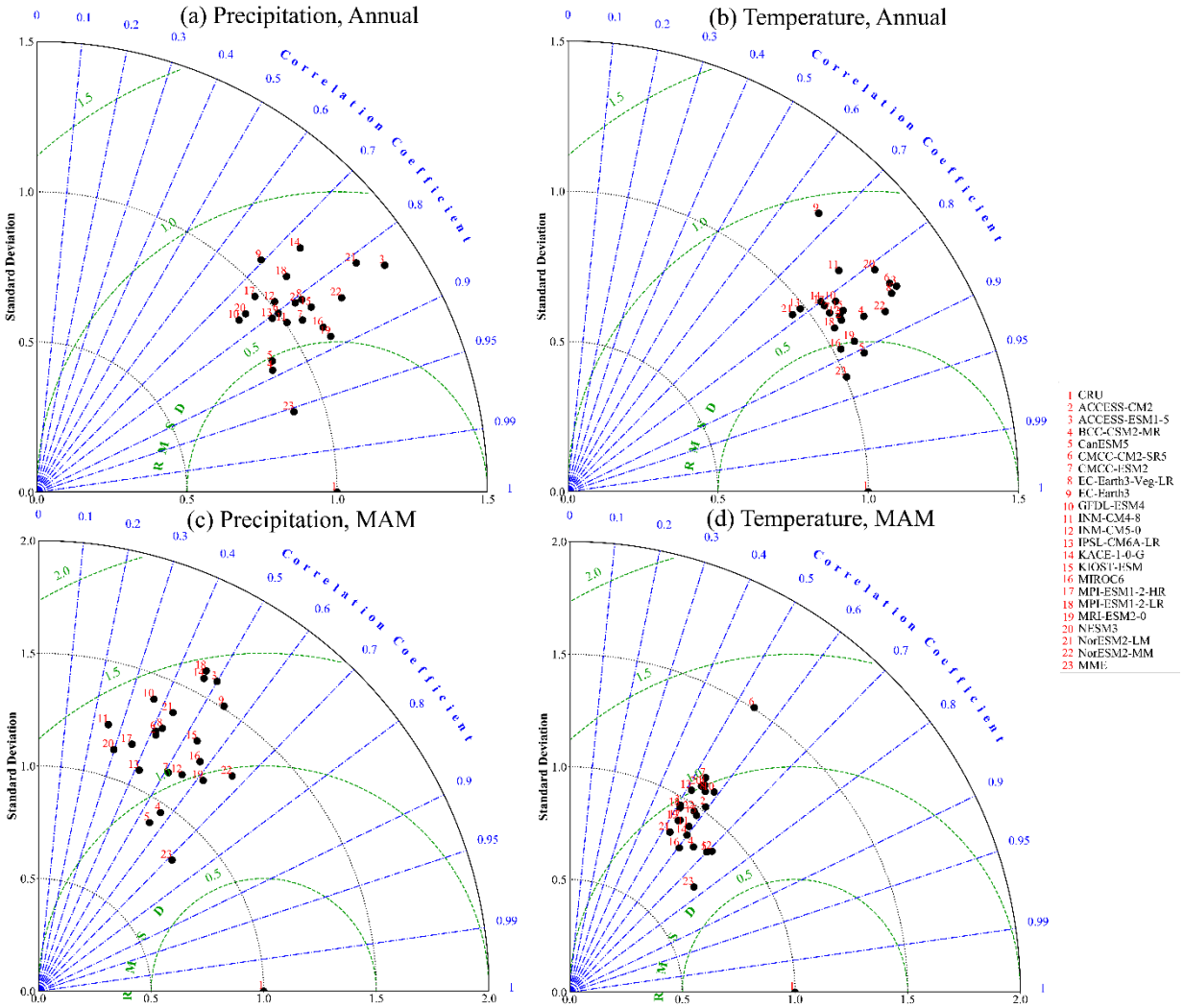

Figure 5. Taylor diagrams comparing CMIP6 observations (1981–2014) for (**a**) annual precipitation; (**b**) annual temperature; (**c**) MAM precipitation; (**d**) MAM temperature. Red represents CMIP6 models, blue lines indicate the correlation coefficient, green lines show RMSD and black lines represent the standard deviation.

In the analysis, an MME was constructed to analyze future changes. The best five models for annual and MAM precipitation and temperature have been selected to compute the MME for projections, as summarized in Table 1.

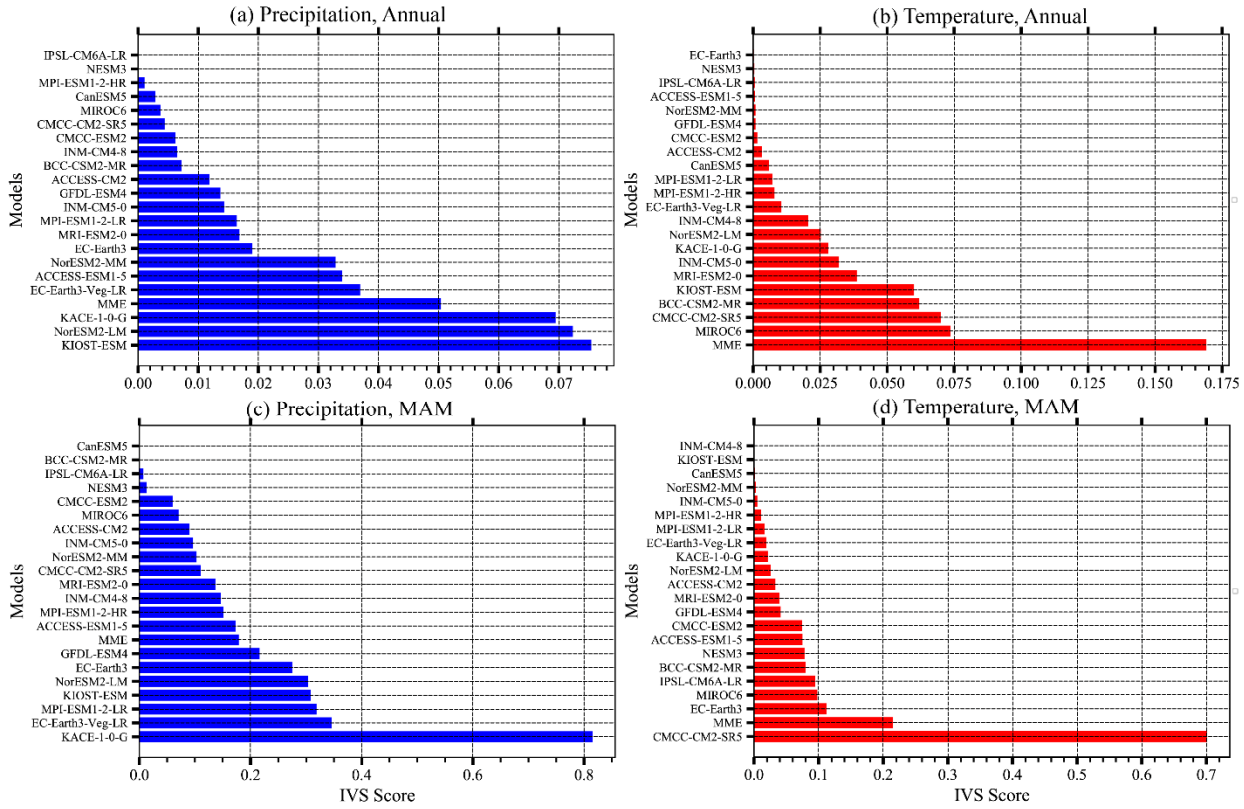

Figure 6. Interannual variability skill score (IVS) of the CMIP6 models for both annual and MAM, (**a**,**c**) precipitation, and (**b**,**d**) temperature over EA. Blue represents CMIP6 models for precipitation, while red represents CMIP6 models for temperature.

3.3. The Future Changes and Trends of Precipitation and Temperature

3.3.1. Projected Changes

To evaluate the reliability between GCMs projections of the future, we computed MME for SSP1-2.6, SSP2-4.5, and SSP5-8.5 scenarios and considered two different periods; near (2031–2065) and far (2066–2100) terms. Figure 7 displays the temporal evolution of annual mean precipitation and temperature from the best-performing models under SSP1-2.6, SSP2-4.5, and SSP5-8.5 scenarios over EA. The annual mean precipitation is projected to rise under SSP5-8.5 from 2040 to 2100, in contrast to other scenarios where a decline is observed from after 2020 to 2040 such as in the SSP1-2.6 scenario. Conversely, under the SSP2-4.5 scenario, precipitation tends to stabilize effectively across various periods. It was quite clear that for SSP1-2.6, annual mean temperature indicates a consistent upward trend up to 2050, followed by a slight cooling thereafter until 2080, and subsequent decline until 2100. Conversely, under SSP2-4.5 and SSP5-8.5, temperatures are projected to steadily rise from 2020 until 2100 with SSP5-8.5 experiencing warming starting post-2020. In summary, the findings reveal an increase in both annual precipitation and temperature in the future, particularly under SSP5-8.5. This agrees with previous studies [87,88], which observed an anticipated rise in annual precipitation and temperature by the end of the twenty-first century under SSP5-8.5 compared to SSP2-4.5 over China.

This cooling pattern is not observed in the other scenarios, where temperatures continue to rise without interruption.

Figure 8 displays the time series of MAM mean precipitation and temperature from the best-performing models under SSP1-2.6, SSP2-4.5, and SSP5-8.5 scenarios over EA. The projections indicate a 40% increase in MAM precipitation and a 4.5 °C rise in temperature under SSP5-8.5 by the end of the century. Furthermore, the study found a decline in MAM precipitation and temperature of 5% and 0.8 °C under SSP2-4.5 and SSP1-2.6, respectively.

No doubt, there is an expected increase in the trend of MAM precipitation and temperature as the 21st century ends under SSP5-8.5 compared to other scenarios.

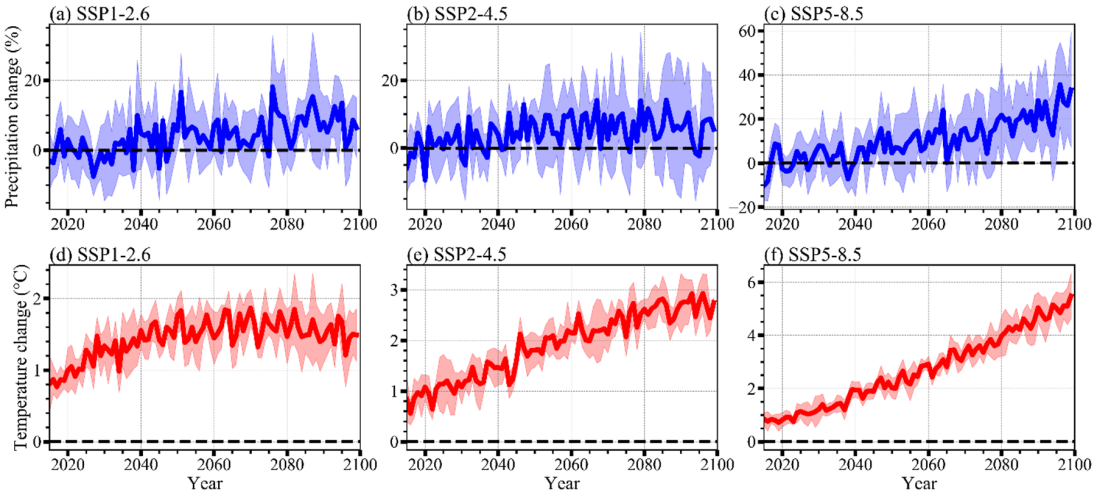

Figure 7. Time series of the annual mean precipitation and temperature from the best-performing models under SSP1-2.6, SSP2-4.5, and SSP5-8.5 scenarios over EA. The blue and red shadings are the corresponding model spread about the MME for the near (2031–2065) and far (2066–2100) terms.

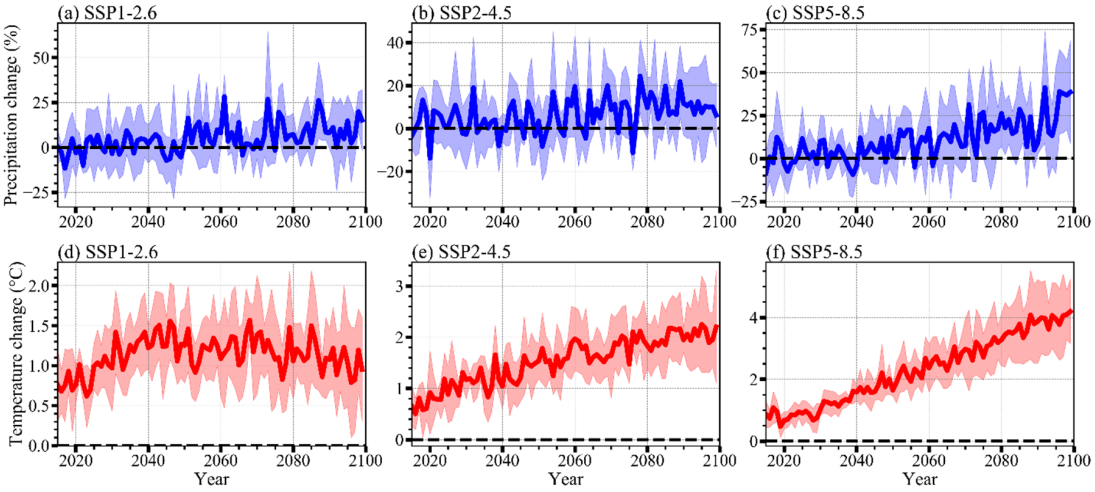

Figure 8. Time series of the MAM mean precipitation and temperature from the best-performing models under SSP1-2.6, SSP2-4.5, and SSP5-8.5 scenarios over EA. The blue and red shadings are the corresponding model spread about the MME for the near (2031–2065) and far (2066–2100) terms.

In Figure 9, the spatial patterns depict the anticipated variations in annual and MAM precipitation derived from MME of CMIP6 models. The projections cover the near-term (2031–2065) and far-term (2066–2100) periods under various scenarios, including SSP1-2.6, SSP2-4.5, and SSP5-8.5. Across all the future scenarios, the projections designate a prevalent increase in precipitation in most areas, with few exceptions showing a reduction in some places. Generally, there is an anticipation of increased precipitation towards the northeast of the EA region. The extent of this rise is notably more substantial under the SSP5-8.5 scenario in contrast to the other scenarios. Conversely, the projected precipitation demonstrates a consistent reduction over the western, eastern, and smaller southern regions of the area. There is a clear lowest decrease in projected changes in MAM precipitation for the near term in Rwanda toward the west, south, and northwestern parts of Uganda, Burundi toward and northwest of Tanzania under SSP2-4.5. Similar precipitation patterns are replicated under SSP5-8.5 for the western part of Tanzania and the southwest part

of Kenya. Furthermore, under SSP1-2.6, the southern, mid-east of Tanzania toward the south of Kenya is projected to receive less precipitation. The highest mean precipitation was observed during the period 2066–2100, with an increase of 20–60% in annual (SSP5-8.5) and MAM (SSP5-8.5). In addition, regions surrounding Lake Victoria in northern Tanzania and the mid-northern Uganda region are expected to experience an annual precipitation increase ranging from 5% to 20% under the SSP5-8.5 scenario. Lake Victoria is recognized as a factor influencing the regional distribution of rainfall in the northern regions of Tanzania [89,90]. Interestingly, results showed that annual and MAM precipitation percentages are predominantly projected to rise in the northern and eastern parts of Kenya in the far term under the SSP5-8.5 scenario.

On the other hand, in all climate scenarios (SSP1-2.6, SSP2-4.5, and SSP5-8.5), the mean precipitation increased during the far term relative to the near term. Notably the highest mean precipitation is predicted to happen in the northern part of Kenya reliable to the study by [29]. The MAM precipitation presented a decrease in the western part of Uganda, Rwanda, and Burundi particularly in the near term under all scenarios. Similarly, the annual precipitation in all periods under all scenarios. Such changes could influence the growing season for food crops across the equatorial EA region since March has been recognized as the onset of the planting season. During the far term, MAM precipitation is anticipated to rise significantly in the extensive region of Kenya, especially under SSP5-8.5, and decrease in the western part of Uganda under SSP1-2.6 and SSP2-4.5 respectively. Overall, the future projections indicate that the northern and eastern parts of Kenya will exhibit notably increased precipitation compared to the baseline period. This contradicts previous studies [91] identified that Kenya will be drier during MAM, particularly in the eastern part.

In general, the utmost substantial positive alteration in mean precipitation is expected to arise in the northern region of Kenya, particularly surrounding the vicinity of the Marsabit Forest Reserve, characterized by a sub-humid mountain forest. Earlier research findings found an increase in both the quantity and distribution of precipitation corresponding with rising radiative forcing [92]. Related studies revealed similar results e.g., [93] but using CMIP5 models. Projections suggest that precipitation in extensive areas of the region will surpass the historical levels throughout the 21st century, aligning with the findings from previous studies based on both RCMs and GCMs [94,95].

Figure 10 illustrates the spatial distributions of changes in annual and MAM temperature derived from the MME of CMIP6 models for the near and far-term scenarios under SSP1-2.6, SSP2-4.5, and SSP5-8.5. The findings indicate enhanced warming over the EA during both near and far-term periods under all three future scenarios. The increase with much stronger warming arises in the high emission SSP5-8.5 scenario for both annual and MAM during the 2066–2100 period exceeding 5 °C. Overall, for SSP1-2.6, SSP2-4.5, and SSP5-8.5 scenarios, the anticipated rise in mean temperature in EA is forecasted to fall between 0.0–2.5 °C, 0.5–3.5 °C and 1.0–5.0 °C respectively. The highest annual temperature is expected to occur in northern, western Kenya, and southwest Tanzania under the SSP5-8.5 scenario during the far-term (2066–2100). While the highest MAM temperature is predicted to occur in central Tanzania. The diminished precipitation over central Tanzania is related to being situated in extensive lowlands [71]. In contrast, the MAM temperature predictions recognized on the SSP1-2.6 scenario during the far term indicate minimum warming in the utmost parts of Uganda, northwest of Kenya, and east-central west of Kenya towards the northeast parts of Tanzania. Particularly, the MAM predictions recognized on the SSP1-2.6 during the far term show a minimal warning with net change not higher than 0 °C (Figure 10j). The lowest temperature was observed in the mountainous areas around Mt. Kenya [92]. Ref. [96] suggests that increased melting brought on by radiative energy gains is the cause of the observed glacier losses on Mt Kenya. Consistent with the observed changes, the projections indicate a rise in extreme climatic events. In addition, the annual temperature was constant in the whole region at the range of 1.5–2.0 °C under SSP2-4.5 during the near term. Substantial and uniform warming surpassing 3.0 °C is anticipated

across the entire region under the SSP2-4.5. The projections under the SSP5-8.5 scenario consistently indicate rising temperatures across the entire predicted period. In agreement with other studies, ref. [32] revealed a homogenous warming which is expected in the whole EA exceeding 7 °C. During the late century, temperature variations are expected to have repercussions on various sectors for instance agriculture, social infrastructure, health, and energy. Regions in Africa including EA are calling for vigorous policy changes considering the projected global warming and the required adaptation [91] to prevent the loss of life and assets.

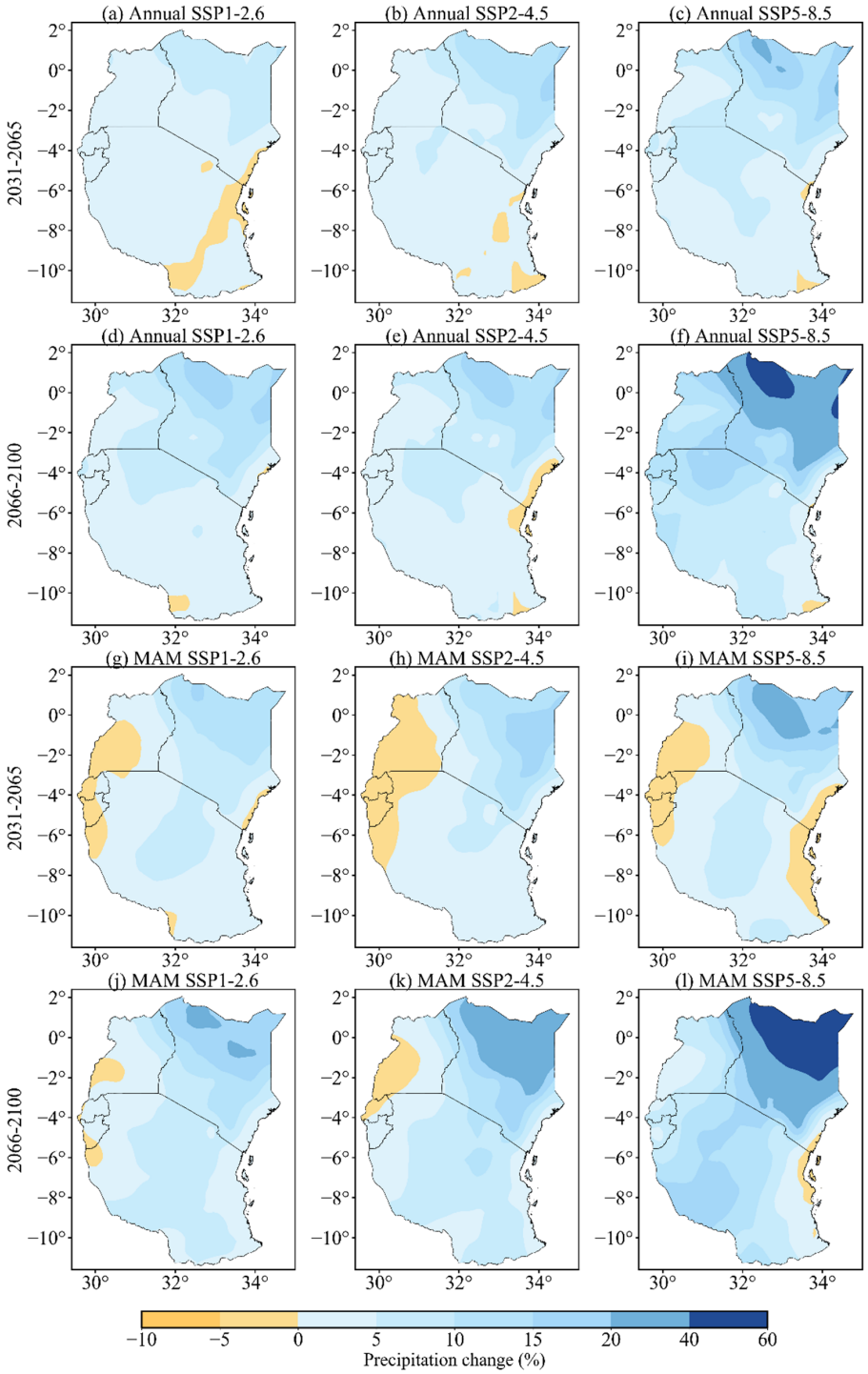

Figure 9. Spatial distributions of changes in annual (**a**–**f**) and MAM (**g**–**l**) precipitation (unit: %) in the near-term (2031–2065) and far-term (2066–2100) relative to historical 1981–2014 over EA under SSP1-2.6, SSP2-4.5, and SSP5-8.5 respectively.

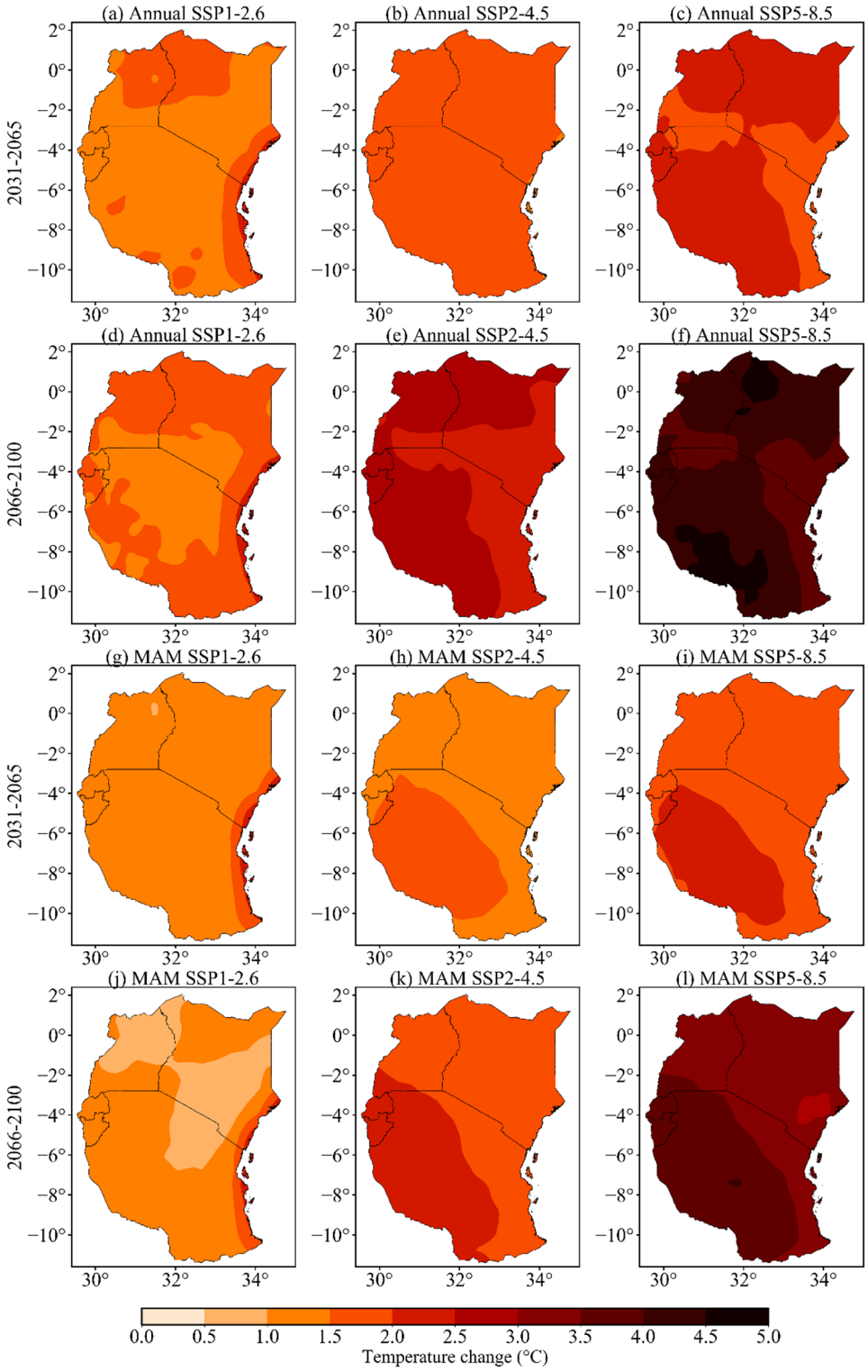

Figure 10. Spatial distribution of changes in annual (**a**–**f**) and MAM (**g**–**l**) temperature (unit: °C) in the near-term (2031–2065) and far-term (2066–2100) relative to historical 1981–2014 over EA under SSP1-2.6, SSP2-4.5, and SSP5-8.5 scenarios respectively.

3.3.2. Projected Trends

The mMK test was used over the study area for future periods, to detect the importance of the estimated trends and potential changes in annual and MAM precipitation as well as temperature throughout SSP1-2.6, SSP2-4.5, and SSP5-8.5 scenarios. Figures 11 and 12 present the spatial trends, whereas Table 2 shows a summary of statistical metrics.

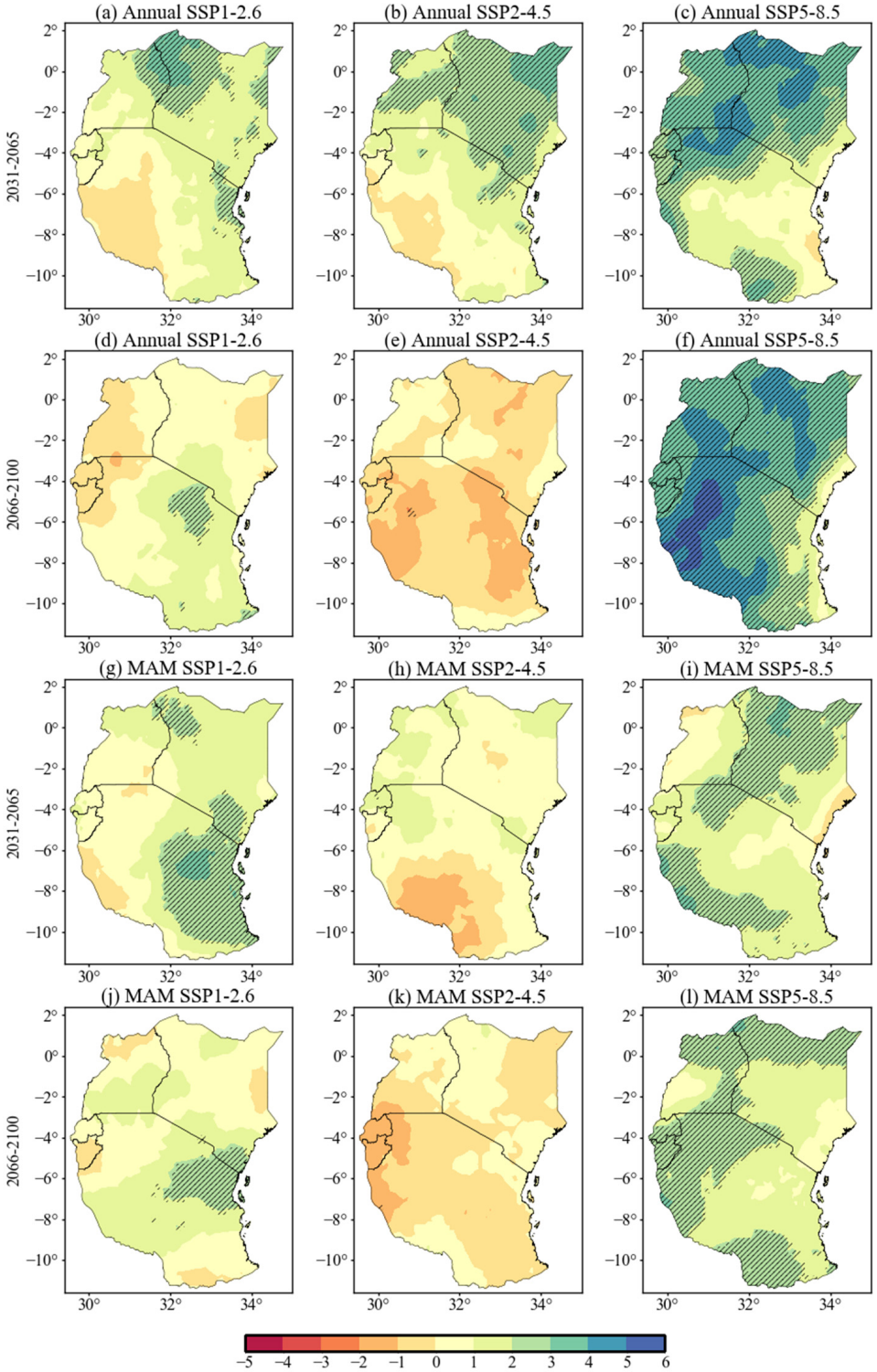

Figure 11. Projected spatial trends of annual (**a**–**f**) and MAM (**g**–**l**) precipitation (unit: mm/year) relative to historical under SSP1-2.6, SSP2-4.5, and SSP5-8.5 respectively over EA. The black dots show changes that are statistically significant with a 95% confidence level.

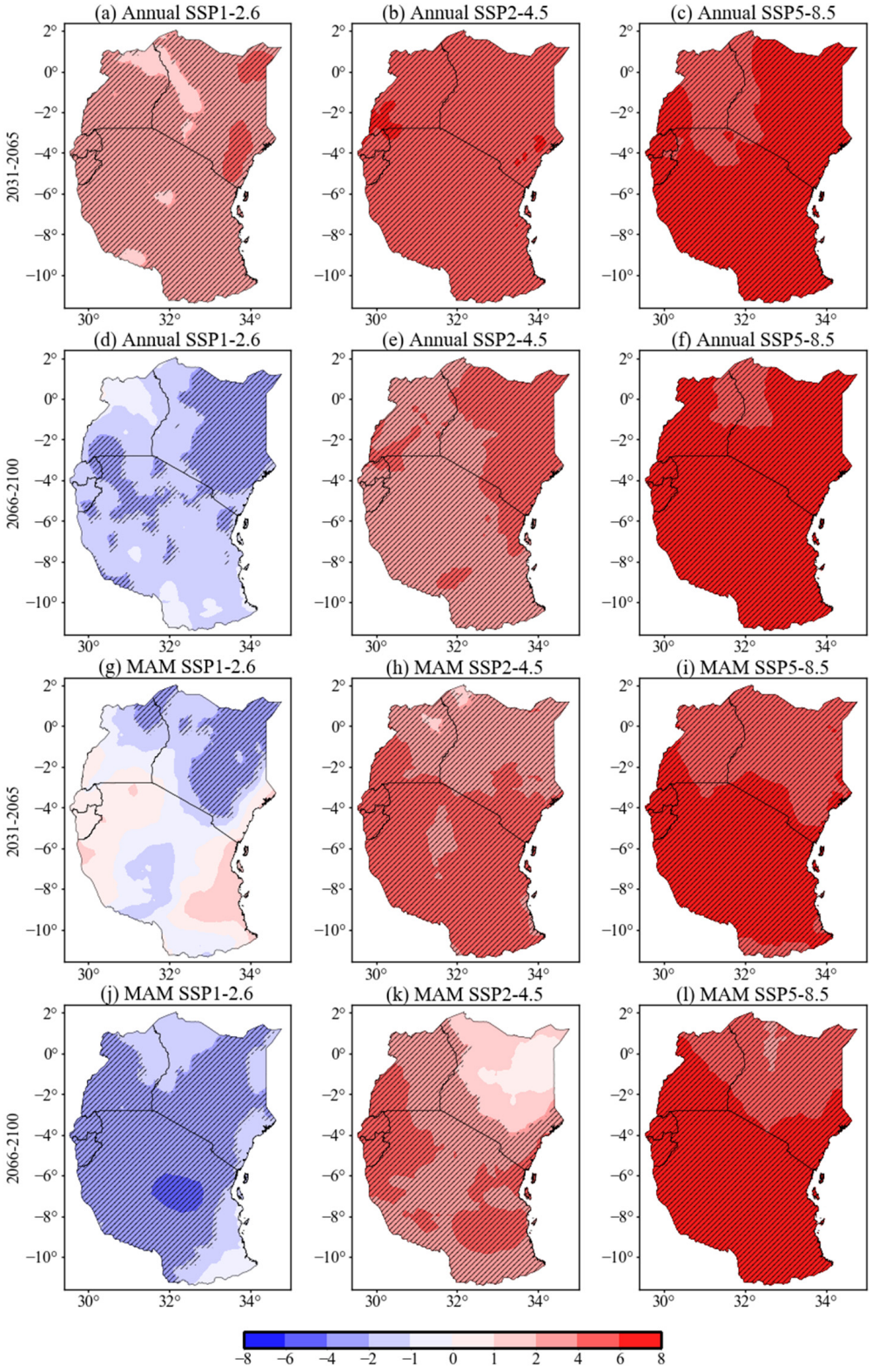

Figure 12. Projected spatial trends of annual (**a**–**f**) and MAM (**g**–**l**) temperature (unit: °C) relative to historical under SSP1-2.6, SSP2-4.5, and SSP5-8.5, respectively, over EA. The black dots show changes that are statistically significant with a 95% confidence level.

Table 2. A description of Sen's Slope Estimator statistics and the modified Mann-Kendall test (mMK) under SSP1-2.6, SSP2-4.5, and SSP5-8.5 scenarios for both annual and MAM seasons.

			Precipitation			Temperature		
			Slope	**z-Value**	***p*-Value**	**Slope**	**z-Value**	***p*-Value**
2031–2064	Annual	SSP1-2.6	0.1188	1.7789	0.0753	0.0112	4.1508	0
		SSP2-4.5	0.1625	2.4609	0.0139	0.032	5.7519	0
		SSP5-8.5	0.3225	4.0026	0.0001	0.0215	6.5821	0
	MAM	SSP1-2.6	0.1943	1.3935	0.1635	−0.0003	−0.1779	0.8588
		SSP2-4.5	0.0626	0.5337	0.5936	0.0226	4.6252	0
		SSP5-8.5	0.4274	2.698	0.007	0.0443	6.5228	0
2065–2100	Annual	SSP1-2.6	0.1316	1.7196	0.0855	−0.0061	−2.0161	0.0438
		SSP2-4.5	−0.0285	−0.4151	0.6781	0.0173	4.2991	0
		SSP5-8.5	0.4937	4.7142	0	0.0667	6.9378	0
	MAM	SSP1-2.6	0.3645	2.3423	0.0192	−0.0096	−2.7573	0.0058
		SSP2-4.5	−0.0195	-0.1186	0.9056	0.0139	4.0619	0
		SSP5-8.5	0.6471	2.3126	0.0207	0.0461	6.6117	0

The anticipated spatial variations in annual precipitation across EA for the periods 2031–2065 and 2066–2100 based on MME under three scenarios are displayed in Figure 11. The analysis displays a rise in precipitation under SSP5-8.5 related to other scenarios. In the MAM season, the spatial trends of precipitation rise over the southwest and northern parts of Tanzania and show different changes over Uganda during the near future under SSP5-8.5. For instance, the annual precipitation results reveal an upward trend with a Z value of 4.0026 in the near term (2031–2065) under SSP5-8.5 (Table 2). Similarly, the MAM precipitation indicates a substantial increase with a Z value of 2.698, also observed under SSP5-8.5 during the same near-term period (2031–2065) (Table 2). Precipitation trends in the northern and eastern regions of Uganda, as well as the western and northern parts of Kenya, are depicted in the far future (2066–2100). During this period, we also observed an increase in precipitation trends in the southwest, the northern part of Tanzania, and the northwest part towards Burundi and Rwanda in the southern parts. However, annual projections for the far future (2066–2100) under SSP5-8.5 reveal a substantial increasing trend covering the entire area, especially the southwestern regions of Tanzania, southern Uganda, and some Kenyan regions. However, SSP5-8.5 during the near future (2031–2065) reveals a significantly increasing trend of annual precipitation in the northwest part of Kenya; the northern part of Tanzania and some parts of Uganda show slightly increasing patterns in some southwest parts of Tanzania.

On the other hand, all SSP2-4.5 expected during 2031–2065 showed that there is no significant trend projected in MAM or at an annual scale. Under SSP1-2.6, certain parts of the area projected a weak trend in both annual and MAM seasons during the far future (2066–2100), as depicted in (Figure 11d,j). For the annual precipitation, the SSP2-4.5 scenario indicates a higher negative value of -2 mm year^{-1} mainly over the western and eastern regions of Tanzania and some parts of Kenya during the long term. For MAM precipitation, a higher negative value of -2 mm year^{-1} was also found in SSP2-4.5, mostly in Rwanda and Burundi and some parts of Tanzania and Uganda. On the other hand, a high positive value of 6 mm year^{-1} was found in annual SSP5-8.5 during the long term in western Tanzania. However, under SSP5-8.5, both annual and MAM precipitation showed high Z values of 4.7142 and 2.3126, respectively, during the far term 2066–2100 (Table 2). In the far term 2066–2100, the findings of the SSP5-8.5 scenario indicated an uptrend in both the annual and MAM precipitation for the entire area (Figure 11f,l).

Figure 12 shows the annual and MAM temperature trends and carries out the significance of EA. Both annual and MAM temperatures exhibit significant increases for both the near-term and the long-term over the whole country, under the SSP5-8.5 scenario, (Figure 12). On the other hand, annual and MAM temperatures exhibited a high Z-value across all scenarios, in both near-term (2031–2065) and far-term (2066–2100) (Table 2). Fur-

ther analysis showed that under the SSP5-8.5 scenario, the temperature rise in the majority of regions across the area exceeds 2–6 °C, and the most rapid warming with a trend of more than 6 °C, is observed in most parts of the region except certain northern parts around Uganda and Kenya. The Z-values for annual and MAM temperatures for both near-term and far-term were 6.5821, 6.5228, 6.9378, and 6.6117, respectively (Table 2). In addition, under SSP2-4.5, it can be seen that annual temperature significantly increased in the whole region in both the near and far term, whereas MAM temperature presents no significant trend in some regions, such as some northeastern parts of Uganda and the small north part of Kenya, in the near term. Similarly, large areas of Kenya also show a declining trend in the far term.

The near-term projections under the SSP1-2.6 scenarios show a decreasing trend in annual temperature across most areas. Interestingly, in the near term, under the SSP1-2.6, the MAM temperature shows a declining trend excluding the central western parts and eastern south part of the area, but only rare areas pass the trend significance at the 95% confidence level. No significant trends were found in Tanzania, Rwanda, Burundi, and some parts of Uganda in MAM under SSP1-2.6 in the near term. Obviously, for the far term (2066–2100), under SSP1-2.6 the MAM temperature displays a declining trend in Tanzania of less than −4 °C. In the near term, the SSP2-4.5 exhibits annual temperature increases across most regions when compared to the SSP1-2.6. However, under SSP1-2.6 an exception is observed in the decrease in annual temperature in the far term and MAM temperature in both the near and far term. In the far term under the SSP1-2.6 scenario, the temperature is statistically decreasing, with the projected trends showing Z values of −2.0161 and −2.7573 for both annual and MAM, respectively (Table 2). In contrast, the fast temperature rises under the SSP5-8.5 scenario above 6 °C with Z values of 6.5821, 6.5228, 6.9378, and 6.6117; respectively, for both annual and MAM near and far (Table 2). Past studies [94,96] similarly indicated that temperatures in the African tropics will increase under the high emissions scenario, using CMIP6 models.

4. Conclusions

Globally, climate change is poised to influence socioeconomic progression, with developing nations being the most impacted. Understanding future climate patterns is crucial for effective planning. This study examined an MME comprised of 21 NEX-GDPP-CMIP6 models, analyzing observed and projected changes in precipitation and temperature across EA during the twenty-first-century end. The assessments considered best performers' models for near-term (2031–2065) and far-term (2066–2100) periods compared to the baseline climate (1981–2014). Projections were made under various emission scenarios, including SSP1-2.6, SSP2-4.5, and SSP5-8.5. The findings indicated a rise in both precipitation and temperature throughout the 21st century. The study underscored the NEX-GDPP-CMIP6 models' effectiveness in accurately depicting the spatial distribution and temporal variations of precipitation and temperature climatology in EA. Considering the overall performance of the two previously mentioned variables, the MME was chosen as the "highest-ranked" model. Therefore, the MME enhanced performance relative to most individual models, and this indicates the importance of incorporating the MME in forecasting and early warning systems over EA.

The study also examined predicted spatial changes and trends in precipitation and temperature from past SSP simulations. The findings indicated that under the SSP5-8.5 scenario, the temperature rise exceeded 2–6 °C in utmost regions across the area, and the fastest warming with an upward trend of more than 6 °C in most parts of the region except in some northern parts around Uganda and Kenya. Furthermore, the projected precipitation increase will be higher under the SSP5-8.5 scenario than under the SSP1-2.6 and SSP2-4.5 scenarios over EA. The predicted rise in precipitation in the EA region is likely to result in more frequent and strengthened extreme climate events, including heavy rainfall linked to floods, which may lead to substantial social and economic losses. Ref. [29] suggested that although precipitation is projected to rise in the region, a decline in soil

moisture content due to warming may result from a decrease in agriculture production. Otherwise, the projected increase in MAM precipitation could provide support to farmers who depend solely on the precipitation for their agricultural endeavors.

Notably, this study is among the first assessments of an ensemble of high spatial resolution NEX-GPDD-CMIP6 climate models. Therefore, their outputs are particularly well suited for application in adaptation studies in various sectors over EA. It provides first-hand information based on most latest updates to climate models and helps provide information about the regional patterns of estimated precipitation and temperature. Future studies may focus on assessments such as land use, the prospect of the most hazardous extreme hydrology, and climate change like droughts and floods in EA.

Supplementary Materials: The following supporting information can be downloaded at: https://www.mdpi.com/article/10.3390/atmos15121455/s1, Table S1: List of selected GCMs from CMIP6 used in the study.

Author Contributions: Conceptualization, E.D.U. and B.O.A.; methodology, E.D.U.; software, E.D.U. and H.B.; validation, E.D.U. and H.B.; formal analysis, E.D.U., B.O.A. and H.B.; investigation, D.I.; resources, D.I.; data curation, E.D.U.; writing—original draft preparation, E.D.U.; writing—review and editing, E.D.U., B.O.A., R.M. and D.M.; visualization, E.D.U., B.O.A., R.M. and D.M.; supervision, X.C.; project administration, X.C.; funding acquisition, X.C. All authors have read and agreed to the published version of the manuscript.

Funding: This study received financial support from the Tianshan Talent Project of Xinjiang Uygur Autonomous Region, China [Grant number 2022TSYCLJ0056].

Institutional Review Board Statement: Not applicable.

Informed Consent Statement: Not applicable.

Data Availability Statement: The source of all the datasets used in the study is provided in the dataset part of the manuscript.

Acknowledgments: The authors extend their gratitude to data centers, including the Climate Research Unit (CRU), for the observed data and latest outputs from NASA Earth Exchange Global Daily Downscaled Projections (NEX-GDDP-CMIP6). We further acknowledge the sponsorship of the Chinese Government Scholarship from the Chinese Academy of Sciences (CAS) and the support provided by the Xinjiang Institute of Ecology and Geography (XIEG), CAS.

Conflicts of Interest: The authors declare no competing of interest.

References

1. Li, S.Y.; Miao, L.J.; Jiang, Z.H.; Wang, G.J.; Gnyawali, K.R.; Zhang, J.; Zhang, H.; Fang, K.; He, Y.; Li, C. Projected drought conditions in Northwest China with CMIP6 models under combined SSPs and RCPs for 2015–2099. *Adv. Clim. Chang. Res.* **2020**, *11*, 210–217. [CrossRef]
2. Degefu, M.A.; Bewket, W. Variability and trends in rainfall amount and extreme event indices in the Omo-Ghibe River Basin, Ethiopia. *Reg. Environ. Chang.* **2014**, *14*, 799–810. [CrossRef]
3. Masson-Delmotte, V.; Zhai, P.; Pörtner, H.; Roberts, D.; Skea, J.; Shukla, P.R.; Pirani, A.; Moufouma-Okia, W.; Péan, C.; Pidcock, R. An IPCC Special Report on the impacts of global warming of 1.5 C above pre-industrial levels and related global greenhouse gas emission pathways, in the context of strengthening the global response to the threat of climate change, sustainable development, and efforts to eradicate poverty. In *Sustainable Development, and Efforts to Eradicate Poverty*; IPCC: Geneva, Switzerland, 2018; p. 630.
4. Stocker, T.F.; Qin, D.; Plattner, G.-K.; Alexander, L.V.; Allen, S.K.; Bindoff, N.L.; Bréon, F.-M.; Church, J.A.; Cubasch, U.; Emori, S. Technical summary. In *Climate Change 2013: The Physical Science Basis*; Contribution of Working Group I to the Fifth Assessment Report of the Intergovernmental Panel on Climate Change; Cambridge University Press: Cambridge, UK, 2013; pp. 33–115. [CrossRef]
5. Bazaz, A.; Bertoldi, P.; Buckeridge, M.; Cartwright, A.; de Coninck, H.; Engelbrecht, F.; Jacob, D.; Hourcade, J.-C.; Klaus, I.; de Kleijne, K. *Summary for Urban Policymakers: What the IPCC Special Report on Global Warming of 1.5 °C Means for Cities*; IPCC: Geneva, Switzerland, 2018.
6. Sharma, S.; Hamal, K.; Khadka, N.; Ali, M.; Subedi, M.; Hussain, G.; Ehsan, M.A.; Saeed, S.; Dawadi, B. Projected drought conditions over Southern slope of the Central Himalaya using CMIP6 models. *Earth Syst. Environ.* **2021**, *5*, 849–859. [CrossRef]

7. Huo-Po, C.; Jian-Qi, S.; Xiao-Li, C. Future changes of drought and flood events in China under a global warming scenario. *Atmos. Ocean. Sci. Lett.* **2013**, *6*, 8–13. [CrossRef]
8. Almazroui, M.; Saeed, F.; Saeed, S.; Nazrul Islam, M.; Ismail, M.; Klutse, N.A.B.; Siddiqui, M.H. Projected change in temperature and precipitation over Africa from CMIP6. *Earth Syst. Environ.* **2020**, *4*, 455–475. [CrossRef]
9. Choi, Y.-W.; Campbell, D.J.; Eltahir, E.A. Near-term regional climate change in East Africa. *Clim. Dyn.* **2023**, *61*, 961–978. [CrossRef]
10. Mwampamba, T.H.; Abrams, R.W.; Awoyemi, S.; Babalola, F.D.; Borokini, T.I.; Egoh, B.; Rguibi Idrissi, H.; Koussa, T.; Nganje, M.; O'Leary, J. The implications of globalization for conservation in Africa. *Afr. J. Ecol.* **2016**, *54*, 133–135. [CrossRef]
11. Allam, M.M.; Eltahir, E.A. Water-energy-food nexus sustainability in the Upper Blue Nile (UBN) Basin. *Front. Environ. Sci.* **2019**, *7*, 5. [CrossRef]
12. Kruger, A.C. Africa and the Paris agreement. *Nat. Clim. Chang.* **2018**, *8*, 365–366. [CrossRef]
13. Ayanlade, A.; Oluwaranti, A.; Ayanlade, O.S.; Borderon, M.; Sterly, H.; Sakdapolrak, P.; Jegede, M.O.; Weldemariam, L.F.; Ayinde, A.F. Extreme climate events in sub-Saharan Africa: A call for improving agricultural technology transfer to enhance adaptive capacity. *Clim. Serv.* **2022**, *27*, 100311. [CrossRef]
14. Bornemann, F.J.; Rowell, D.P.; Evans, B.; Lapworth, D.J.; Lwiza, K.; Macdonald, D.M.; Marsham, J.H.; Tesfaye, K.; Ascott, M.J.; Way, C. Future changes and uncertainty in decision-relevant measures of East African climate. *Clim. Chang.* **2019**, *156*, 365–384. [CrossRef]
15. Opiyo, F.; Wasonga, O.; Nyangito, M.; Schilling, J.; Munang, R. Drought adaptation and coping strategies among the Turkana pastoralists of northern Kenya. *Int. J. Disaster Risk Sci.* **2015**, *6*, 295–309. [CrossRef]
16. Kumar, N.; Goyal, M.K.; Gupta, A.K.; Jha, S.; Das, J.; Madramootoo, C.A. Joint behaviour of climate extremes across India: Past and future. *J. Hydrol.* **2021**, *597*, 126185. [CrossRef]
17. Niggli, L.; Huggel, C.; Muccione, V.; Neukom, R.; Salzmann, N. Towards improved understanding of cascading and interconnected risks from concurrent weather extremes: Analysis of historical heat and drought extreme events. *PLoS Clim.* **2022**, *1*, e0000057. [CrossRef]
18. Taylor, K.E.; Stouffer, R.J.; Meehl, G.A. An overview of CMIP5 and the experiment design. *Bull. Am. Meteorol. Soc.* **2012**, *93*, 485–498. [CrossRef]
19. Kamruzzaman, M.; Wahid, S.; Shahid, S.; Alam, E.; Mainuddin, M.; Islam, H.T.; Cho, J.; Rahman, M.M.; Biswas, J.C.; Thorp, K.R. Predicted changes in future precipitation and air temperature across Bangladesh using CMIP6 GCMs. *Heliyon* **2023**, *9*, e16274. [CrossRef]
20. Yue, S.; Pilon, P.; Phinney, B.; Cavadias, G. The influence of autocorrelation on the ability to detect trend in hydrological series. *Hydrol. Process.* **2002**, *16*, 1807–1829. [CrossRef]
21. Dixit, S.; Atla, B.M.; Jayakumar, K. Evolution and drought hazard mapping of future meteorological and hydrological droughts using CMIP6 model. *Stoch. Environ. Res. Risk Assess.* **2022**, *36*, 3857–3874. [CrossRef]
22. Salunke, P.; Keshri, N.P.; Mishra, S.K.; Dash, S. Future projections of seasonal temperature and precipitation for India. *Front. Clim.* **2023**, *5*, 1069994. [CrossRef]
23. Eyring, V.; Bony, S.; Meehl, G.A.; Senior, C.A.; Stevens, B.; Stouffer, R.J.; Taylor, K.E. Overview of the Coupled Model Intercomparison Project Phase 6 (CMIP6) experimental design and organization. *Geosci. Model Dev.* **2016**, *9*, 1937–1958. [CrossRef]
24. Scafetta, N. CMIP6 GCM ensemble members versus global surface temperatures. *Clim. Dyn.* **2023**, *60*, 3091–3120. [CrossRef]
25. Kamworapan, S.; Thao, P.T.B.; Gheewala, S.H.; Pimonsree, S.; Prueksakorn, K. Evaluation of CMIP6 GCMs for simulations of temperature over Thailand and nearby areas in the early 21st century. *Heliyon* **2021**, *7*, e08263. [CrossRef] [PubMed]
26. Bouramdane, A.-A. Assessment of CMIP6 Multi-Model Projections Worldwide: Which Regions Are Getting Warmer and Are Going through a Drought in Africa and Morocco? What Changes from CMIP5 to CMIP6? *Sustainability* **2022**, *15*, 690. [CrossRef]
27. Chen, H.; Sun, J.; Lin, W.; Xu, H. Comparison of CMIP6 and CMIP5 models in simulating climate extremes. *Sci. Bull.* **2020**, *65*, 1415–1418. [CrossRef] [PubMed]
28. Li, H.; Li, Z.; Chen, Y.; Xiang, Y.; Liu, Y.; Kayumba, P.M.; Li, X. Drylands face potential threat of robust drought in the CMIP6 SSPs scenarios. *Environ. Res. Lett.* **2021**, *16*, 114004. [CrossRef]
29. Ongoma, V.; Chen, H.; Gao, C. Projected changes in mean rainfall and temperature over East Africa based on CMIP5 models. *Int. J. Climatol.* **2017**, *38*, 1375–1392. [CrossRef]
30. Ongoma, V.; Chen, H.; Gao, C.; Nyongesa, A.M.; Polong, F. Future changes in climate extremes over Equatorial East Africa based on CMIP5 multimodel ensemble. *Nat. Hazards* **2018**, *90*, 901–920. [CrossRef]
31. Ayugi, B.; Dike, V.; Ngoma, H.; Babaousmail, H.; Mumo, R.; Ongoma, V. Future changes in precipitation extremes over East Africa based on CMIP6 models. *Water* **2021**, *13*, 2358. [CrossRef]
32. Ayugi, B.; Ngoma, H.; Babaousmail, H.; Karim, R.; Iyakaremye, V.; Sian, K.T.L.K.; Ongoma, V. Evaluation and projection of mean surface temperature using CMIP6 models over East Africa. *J. Afr. Earth Sci.* **2021**, *181*, 104226. [CrossRef]
33. Akinsanola, A.A.; Ongoma, V.; Kooperman, G.J. Evaluation of CMIP6 models in simulating the statistics of extreme precipitation over Eastern Africa. *Atmos. Res.* **2021**, *254*, 105509. [CrossRef]
34. Schwarzwald, K.; Goddard, L.; Seager, R.; Ting, M.; Marvel, K. Understanding CMIP6 biases in the representation of the Greater Horn of Africa long and short rains. *Clim. Dyn.* **2022**, *61*, 1229–1255. [CrossRef]

35. Rowell, D.P.; Booth, B.B.; Nicholson, S.E.; Good, P. Reconciling past and future rainfall trends over East Africa. *J. Clim.* **2015**, *28*, 9768–9788. [CrossRef]
36. Vigaud, N.; Lyon, B.; Giannini, A. Sub-seasonal teleconnections between convection over the Indian Ocean, the East African long rains and tropical Pacific surface temperatures. *Int. J. Climatol.* **2016**, *37*, 1167–1180. [CrossRef]
37. Wainwright, C.M.; Marsham, J.H.; Keane, R.J.; Rowell, D.P.; Finney, D.L.; Black, E.; Allan, R.P. 'Eastern African Paradox'rainfall decline due to shorter not less intense Long Rains. *npj Clim. Atmos. Sci.* **2019**, *2*, 34. [CrossRef]
38. Thrasher, B.; Wang, W.; Michaelis, A.; Melton, F.; Lee, T.; Nemani, R. NASA global daily downscaled projections, CMIP6. *Sci. Data* **2022**, *9*, 262. [CrossRef]
39. Moradian, S.; Iglesias, G.; Broderick, C.; Olbert, I.A. Assessing the impacts of climate change on precipitation through a hybrid method of machine learning and discrete wavelet transform techniques, case study: Cork, Ireland. *J. Hydrol. Reg. Stud.* **2023**, *49*, 101523. [CrossRef]
40. Tang, J.; Song, P.; Hu, X.; Chen, C.; Wei, B.; Zhao, S. Coupled effects of land use and climate change on water supply in SSP–RCP scenarios: A case study of the Ganjiang river Basin, China. *Ecol. Indic.* **2023**, *154*, 110745. [CrossRef]
41. Teixeira, A.L.d.F.; Bhaduri, A.; Siefert, C.A.C.; Iftekhar, M.S.; Bunn, S.E.; de Souza, S.A.; Gonçalves, M.V.C.; da Costa, L.C. Water security threats and solutions in the Grande River basin–One of the Brazilian agricultural frontiers. *Sci. Total Environ.* **2023**, *906*, 167351. [CrossRef]
42. Ojara, M.A.; Yunsheng, L.; Uddin, M.; Babaousmail, H.; Ayugi, B. Statistical Evaluation of Changes and Periodicity in Rainfall Over East Africa During the Period 1960–2017. *Pure Appl. Geophys.* **2022**, *179*, 2969–2992. [CrossRef]
43. Song, Y.; Semazzi, F.H.; Xie, L.; Ogallo, L.J. A coupled regional climate model for the Lake Victoria basin of East Africa. *Int. J. Climatol.* **2004**, *24*, 57–75. [CrossRef]
44. Ntiba, M.; Kudoja, W.; Mukasa, C. Management issues in the Lake Victoria watershed. *Lakes Reserv. Res. Manag.* **2001**, *6*, 211–216. [CrossRef]
45. Ongoma, V.; Chen, H. Temporal and spatial variability of temperature and precipitation over East Africa from 1951 to 2010. *Meteorol. Atmos. Phys.* **2017**, *129*, 131–144. [CrossRef]
46. Adhikari, U.; Nejadhashemi, A.P.; Woznicki, S.A. Climate change and eastern Africa: A review of impact on major crops. *J. Food Energy Secur.* **2015**, *4*, 110–132. [CrossRef]
47. UNICEF. *The State of Food Security and Nutrition in the World 2020*; UNICEF: New York, NY, USA, 2020. [CrossRef]
48. Indeje, M.; Semazzi, F.H.; Ogallo, L.J. ENSO signals in East African rainfall seasons. *Int. J. Climatol.* **2000**, *20*, 19–46. [CrossRef]
49. Ayugi, B.O.; Tan, G. Recent trends of surface air temperatures over Kenya from 1971 to 2010. *Meteorol. Atmos. Phys.* **2019**, *131*, 1401–1413. [CrossRef]
50. Peel, M.C.; Finlayson, B.L.; McMahon, T.A. Updated world map of the Köppen-Geiger climate classification. *Hydrol. Earth Syst. Sci.* **2007**, *11*, 1633–1644. [CrossRef]
51. Wu, F.; Jiao, D.; Yang, X.; Cui, Z.; Zhang, H.; Wang, Y. Evaluation of NEX-GDDP-CMIP6 in simulation performance and drought capture utility over China–based on DISO. *Hydrol. Res.* **2023**, *54*, 703–721. [CrossRef]
52. Golian, S.; El-Idrysy, H.; Stambuk, D. Using CMIP6 Models to Assess Future Climate Change Effects on Mine Sites in Kazakhstan. *Hydrology* **2023**, *10*, 150. [CrossRef]
53. Ghazi, B.; Dutt, S.; Torabi Haghighi, A. Projection of Future Meteorological Droughts in Lake Urmia Basin, Iran. *Water* **2023**, *15*, 1558. [CrossRef]
54. Harris, I.; Osborn, T.J.; Jones, P.; Lister, D. Version 4 of the CRU TS monthly high-resolution gridded multivariate climate dataset. *Sci. Data* **2020**, *7*, 109. [CrossRef]
55. Ayugi, B.; Shilenje, Z.W.; Babaousmail, H.; Lim Kam Sian, K.T.; Mumo, R.; Dike, V.N.; Iyakaremye, V.; Chehbouni, A.; Ongoma, V. Projected changes in meteorological drought over East Africa inferred from bias-adjusted CMIP6 models. *Nat. Hazards* **2022**, *113*, 1151–1176. [CrossRef] [PubMed]
56. Ongoma, V.; Chen, H.; Omony, G.W. Variability of extreme weather events over the equatorial East Africa, a case study of rainfall in Kenya and Uganda. *Theor. Appl. Climatol.* **2018**, *131*, 295–308. [CrossRef]
57. Chen, H.; Liu, H.; Chen, X.; Qiao, Y. Analysis on impacts of hydro-climatic changes and human activities on available water changes in Central Asia. *Sci. Total Environ.* **2020**, *737*, 139779. [CrossRef] [PubMed]
58. Zhang, Y.; You, Q.; Chen, C.; Ge, J.; Adnan, M. Evaluation of downscaled CMIP5 coupled with VIC model for flash drought simulation in a humid subtropical basin, China. *J. Clim.* **2018**, *31*, 1075–1090. [CrossRef]
59. Ayugi, B.; Tan, G.; Gnitou, G.T.; Ojara, M.; Ongoma, V. Historical evaluations and simulations of precipitation over East Africa from Rossby centre regional climate model. *Atmos. Res.* **2020**, *232*, 104705. [CrossRef]
60. Abbas, A.; Ullah, S.; Ullah, W.; Waseem, M.; Dou, X.; Zhao, C.; Karim, A.; Zhu, J.; Hagan, D.F.T.; Bhatti, A.S. Evaluation and projection of precipitation in Pakistan using the Coupled Model Intercomparison Project Phase 6 model simulations. *Int. J. Clim.* **2022**, *42*, 6665–6684. [CrossRef]
61. Taylor, K.E. Summarizing multiple aspects of model performance in a single diagram. *J. Geophys. Res. Atmos.* **2001**, *106*, 7183–7192. [CrossRef]
62. Babaousmail, H.; Hou, R.; Ayugi, B.; Ojara, M.; Ngoma, H.; Karim, R.; Rajasekar, A.; Ongoma, V. Evaluation of the performance of CMIP6 models in reproducing rainfall patterns over North Africa. *Atmosphere* **2021**, *12*, 475. [CrossRef]

63. Ngoma, H.; Wen, W.; Ojara, M.; Ayugi, B. Assessing current and future spatiotemporal precipitation variability and trends over Uganda, East Africa, based on CHIRPS and regional climate model datasets. *Meteorol. Atmos. Phys.* **2021**, *133*, 823–843. [CrossRef]
64. Kendall, M.G. *Rank Correlation Methods*; Griffin: Glasgow, UK, 1948.
65. Sen, P.K. Estimates of the regression coefficient based on Kendall's tau. *J. Amer. Stat. Assoc.* **1968**, *63*, 1379–1389. [CrossRef]
66. Ahmed, K.; Sachindra, D.A.; Shahid, S.; Demirel, M.C.; Chung, E.-S. Selection of multi-model ensemble of general circulation models for the simulation of precipitation and maximum and minimum temperature based on spatial assessment metrics. *J. Hydrol. Earth Syst. Sci.* **2019**, *23*, 4803–4824. [CrossRef]
67. Milinski, S.; Maher, N.; Olonscheck, D. How large does a large ensemble need to be? *Earth Syst. Dyn.* **2020**, *11*, 885–901. [CrossRef]
68. Ongoma, V.; Chen, H.; Gao, C. Evaluation of CMIP5 twentieth century rainfall simulation over the equatorial East Africa. *Theor. Appl. Climatol.* **2019**, *135*, 893–910. [CrossRef]
69. Tokarska, K.B.; Stolpe, M.B.; Sippel, S.; Fischer, E.M.; Smith, C.J.; Lehner, F.; Knutti, R. Past warming trend constrains future warming in CMIP6 models. *Sci. Adv.* **2020**, *6*, eaaz9549. [CrossRef]
70. Camberlin, P. Climate of eastern Africa. In *Oxford Research Encyclopedia of Climate Science*; Oxford University Press: Oxford, UK, 2018. [CrossRef]
71. Mbigi, D.; Onyango, A.O.; Mtewele, Z.F.; Kiprotich, P.; Xiao, Z. Coupled Model Intercomparison Project Phase 6 simulations of the spatial structure of rainfall variability over East Africa: Evaluation and projection. *Int. J. Climatol.* **2022**, *42*, 9865–9885. [CrossRef]
72. Chang'a, L.B.; Yanda, P.Z.; Ngana, J. Spatial and temporal analysis of recent climatological data in Tanzania. *J. Geogr. Reg. Plan.* **2010**, *3*, 44–65.
73. Makula, E.K.; Zhou, B. Coupled Model Intercomparison Project phase 6 evaluation and projection of East African precipitation. *Int. J. Climatol.* **2022**, *42*, 2398–2412. [CrossRef]
74. Ongoma, V.; Chen, H.; Gao, C.; Sagero, P.O. Variability of temperature properties over Kenya based on observed and reanalyzed datasets. *Theor. Appl. Climatol.* **2018**, *133*, 1175–1190. [CrossRef]
75. Pachauri, R.K.; Allen, M.R.; Barros, V.R.; Broome, J.; Cramer, W.; Christ, R.; Church, J.A.; Clarke, L.; Dahe, Q.; Dasgupta, P. *Climate Change 2014: Synthesis Report*; Contribution of Working Groups I, II and III to the fifth Assessment Report of the Intergovernmental Panel on Climate Change; IPCC: Geneva, Switzerland, 2014.
76. Tong, M.; Li, L.; Li, Z.; Tian, Z. Spatiotemporal Analysis of Future Precipitation Changes in the Huaihe River Basin Based on the NEX-GDDP-CMIP6 Dataset and Monitoring Data. *Water* **2023**, *15*, 3805. [CrossRef]
77. Harris, I.; Jones, P.D.; Osborn, T.J.; Lister, D.H. Updated high-resolution grids of monthly climatic observations–the CRU TS3. 10 Dataset. *Int. J. Climatol.* **2013**, *34*, 623–642. [CrossRef]
78. Fan, X.; Duan, Q.; Shen, C.; Wu, Y.; Xing, C. Global surface air temperatures in CMIP6: Historical performance and future changes. *Environ. Res. Lett.* **2020**, *15*, 104056. [CrossRef]
79. Bador, M.; Boé, J.; Terray, L.; Alexander, L.V.; Baker, A.; Bellucci, A.; Haarsma, R.; Koenigk, T.; Moine, M.P.; Lohmann, K. Impact of higher spatial atmospheric resolution on precipitation extremes over land in global climate models. *J. Geophys. Res. Atmos.* **2020**, *125*, e2019JD032184. [CrossRef]
80. Zhu, H.; Jiang, Z.; Li, J.; Li, W.; Sun, C.; Li, L. Does CMIP6 inspire more confidence in simulating climate extremes over China? *Adv. Atmos. Sci.* **2020**, *37*, 1119–1132. [CrossRef]
81. Khadka, D.; Babel, M.S.; Abatan, A.A.; Collins, M. An evaluation of CMIP5 and CMIP6 climate models in simulating summer rainfall in the Southeast Asian monsoon domain. *Int. J. Climatol.* **2022**, *42*, 1181–1202. [CrossRef]
82. Ortega, G.; Arias, P.A.; Villegas, J.C.; Marquet, P.A.; Nobre, P. Present-day and future climate over central and South America according to CMIP5/CMIP6 models. *Int. J. Climatol.* **2021**, *41*, 6713–6735. [CrossRef]
83. Tang, B.; Hu, W.; Duan, A. Assessment of extreme precipitation indices over Indochina and South China in CMIP6 models. *J. Clim.* **2021**, *34*, 7507–7524. [CrossRef]
84. Yue, Y.; Yan, D.; Yue, Q.; Ji, G.; Wang, Z. Future changes in precipitation and temperature over the Yangtze River Basin in China based on CMIP6 GCMs. *Atmos. Res.* **2021**, *264*, 105828. [CrossRef]
85. Wei, L.; Xin, X.; Li, Q.; Wu, Y.; Tang, H.; Li, Y.; Yang, B. Simulation and projection of climate extremes in China by multiple Coupled Model Intercomparison Project Phase 6 models. *Int. J. Climatol.* **2022**, *43*, 219–239. [CrossRef]
86. Tian, D.; Guo, Y.; Dong, W. Future changes and uncertainties in temperature and precipitation over China based on CMIP5 models. *Adv. Atmos. Sci.* **2015**, *32*, 487–496. [CrossRef]
87. Yang, X.; Zhou, B.; Xu, Y.; Han, Z. CMIP6 evaluation and projection of temperature and precipitation over China. *Adv. Atmos. Sci.* **2021**, *38*, 817–830. [CrossRef]
88. Yin, X.; Nicholson, S.E.; Ba, M.B. On the diurnal cycle of cloudiness over Lake Victoria and its influence on evaporation from the lake. *Hydrol. Sci. J.* **2000**, *45*, 407–424. [CrossRef]
89. Borhara, K.; Pokharel, B.; Bean, B.; Deng, L.; Wang, S.-Y.S. On Tanzania's precipitation climatology, variability, and future projection. *Climate* **2020**, *8*, 34. [CrossRef]
90. Gebrechorkos, S.H.; Hülsmann, S.; Bernhofer, C. Regional climate projections for impact assessment studies in East Africa. *Environ. Res. Lett.* **2019**, *14*, 44031. [CrossRef]

91. Ojara, M.A.; Yunsheng, L.; Ongoma, V.; Mumo, L.; Akodi, D.; Ayugi, B.; Ogwang, B.A. Projected changes in East African climate and its impacts on climatic suitability of maize production areas by the mid-twenty-first century. *Environ. Monit. Assess.* **2021**, *193*, 831. [CrossRef] [PubMed]
92. Muhati, G.L.; Olago, D.; Olaka, L. Past and projected rainfall and temperature trends in a sub-humid Montane Forest in Northern Kenya based on the CMIP5 model ensemble. *Glob. Ecol. Conserv.* **2018**, *16*, e00469. [CrossRef]
93. Engelbrecht, F.; Adegoke, J.; Bopape, M.-J.; Naidoo, M.; Garland, R.; Thatcher, M.; McGregor, J.; Katzfey, J.; Werner, M.; Ichoku, C. Projections of rapidly rising surface temperatures over Africa under low mitigation. *Environ. Res. Lett.* **2015**, *10*, 085004. [CrossRef]
94. Cooper, P.; Stern, R.D.; Noguer, M.; Gathenya, J.M. Climate change adaptation strategies in Sub-Saharan Africa: Foundations for the future. In *Climate Change—Realities, Impacts over Ice Cap, Sea Level and Risks*; InTechOpen: London, UK, 2013.
95. Prinz, R.; Nicholson, L.I.; Mölg, T.; Gurgiser, W.; Kaser, G. Climatic controls and climate proxy potential of Lewis Glacier, Mt. Kenya. *Cryosphere* **2016**, *10*, 133–148. [CrossRef]
96. Umugwaneza, A.; Chen, X.; Liu, T.; Li, Z.; Uwamahoro, S.; Mind'je, R.; Dufatanye Umwali, E.; Ingabire, R.; Uwineza, A. Future Climate Change Impact on the Nyabugogo Catchment Water Balance in Rwanda. *Water* **2021**, *13*, 3636. [CrossRef]